3-12-2009

An Investigation of Shock Wave Physics via Hybrid CFD-BGK Solution Methods for Nonequilibrium Flows

Brook I. Bentley

An Investigation of Shock Wave Physics via
Hybrid CFD-BGK Solution Methods for
Nonequilibrium Flows

THESIS

Brook I. Bentley, First Lieutenant, USAF

AFIT/GAE/ENY/09-M02

DEPARTMENT OF THE AIR FORCE
AIR UNIVERSITY

AIR FORCE INSTITUTE OF TECHNOLOGY

Wright-Patterson Air Force Base, Ohio

AFIT/GAE/ENY/09-M02

An Investigation of Shock Wave Physics via Hybrid CFD-BGK Solution Methods for Nonequilibrium Flows

THESIS

Presented to the Faculty

Department of Aeronautics and Astronautics

Graduate School of Engineering and Management

Air Force Institute of Technology

Air University

Air Education and Training Command

In Partial Fulfillment of the Requirements for the

Degree of Master of Science in Aeronautical Engineering

Brook I. Bentley, BS

First Lieutenant, USAF

March 2009

AFIT/GAE/ENY/09-M02

An Investigation of Shock Wave Physics via Hybrid CFD-BGK Solution Methods for Nonequilibrium Flows

Brook I. Bentley, BS
First Lieutenant, USAF

Approved:

/signed/	12 March 2009
Dr. Robert B. Greendyke (Chairman)	Date
/signed/	12 March 2009
Major Richard E. Huffman, PhD (Member)	Date
/signed/	12 March 2009
Major Andrew J. Lofthouse, PhD (Member)	Date

AFIT/GAE/ENY/09-M02

Abstract

The Unified Flow Solver, a hybrid continuum-rarefied code, is used to investigate the internal structure of a normal shock wave for a Mach range of 1.55 to 9.0 for Argon, and 1.53 to 3.8 for diatomic Nitrogen. Reciprocal shock thickness, density, temperature, heat flux, and the velocity distribution function are calculated for a one-dimensional shock wave and compared with experimental data from Alsmeyer and DSMC results from Bird. Using the Euler, Navier-Stokes, BGK model, and Three-Temperature BGK model schemes, results from UFS compare well with experiment and DSMC. The Euler scheme shows atypical results, possibly resulting from modifications made to include internal energies.

An entropy spot is introduced into a two-dimensional domain to investigate entropy-shock interactions over a range of Knudsen numbers ($Kn = 0.01$, 0.1, and 1.0) for Mach 2.0 in Argon. Previous work on entropy-shock interactions has only been performed using an Euler scheme. Here, results are presented in Argon using coupled BGK and Navier-Stokes solvers. Density, pressure, and temperature profiles, as well as the profiles of their gradients, are reported at certain times after the entropy spot convects through the shock.

Acknowledgements

I humbly thank my Heavenly Father for providing needed insight into the equations and theories involved in this work, as well as His merciful support and encouragement. I am also deeply indebted to my great wife and to my two wonderful children for their love and understanding. This work would not have been possible without the helpful guidance, input, and mentoring of my Thesis advisor, Dr. Robert Greendyke. I gratefully acknowledge Dr. Datta Gaitonde, Mr. Eswar Joshula, as well as the Air Vehicles Directorate of the Air Force Research Laboratory (AFRL/RB) for their kind and generous support of this project. My sincere thanks also go to Dr. Robert Arslanbekov and Dr. Vladimir Kolobov from the CFD Research Corporation for their helpful comments regarding the use of UFS, as well as for providing the code required to introduce an entropy spot during a simulation. Finally, I am aware of the great blessing provided to me by my sponsor, AFRL's Directed Energy Directorate, and by the United States Air Force, to be able to pursue my Master's degree at the Air Force Institute of Technology.

Brook I. Bentley

Table of Contents

List of Figures

An Investigation of Shock Wave Physics via Hybrid CFD-BGK Solution Methods for Nonequilibrium Flows

I. Introduction

Hypersonics is a current field of research and interest in the Department of Defense (DoD), the United States Air Force (USAF), and around the world.[1] For example, in 2006 the Hypersonic International Flight Research Experimentation program (HiFire) began with \$54 million of funding and an agreement between USAF and the Australian Department of Defense. HiFire will continue through 2012, providing basic and applied research to better understand hypersonic flows, as well as to generate experimental data. The program will include up to 10 flight experiments (with payload) at realistic hypersonic flight conditions. Seen as a game-changing capability, Douglas Dolvin of the Air Vehicles Directorate of the Air Force Research Laboratory (AFRL) stated,

> We envision air-breathing powered hypersonic cruise missiles in the near-term, which are able to deliver prompt, precision strike of time critical targets from safe, standoff distances. In the far-term, these air-breathing hypersonic vehicles may enable operationally responsive space access. [1]

In order to understand the difficulties associated with hypersonics research, it is important to understand more about hypersonic flows. A flow usually defined as hypersonic if the Mach number is greater than or equal to five ($M \geq 5$), although Anderson has extended the definition to include any flow where certain physical phenomena become important [4].[2] Civilian transport aircraft, such as a Boeing 747, operate in subsonic speeds ($M < 1$) and up to a certain altitude. Due to design concerns, such aircraft do not break the sound barrier, and in practice stay below transonic regimes ($0.8 \leq M \leq 1.2$), where some flow over the aircraft is

---

[1]Lists of symbols and abbreviations are included in the appendices.
[2]Such as a thin shock layer, an entropy layer, strong viscous interaction, high temperatures, and low densities.

supersonic ($M > 1$) and some of the flow is still subsonic. On the other hand, fighter jets, such as the F-22 Raptor, are designed to fly at supersonic speeds, and regularly do so when flying over oceans. At supersonic speeds, shock waves form due to the compressibility effects of the air. At such high velocities, the kinetic energy of the flow can be dissipated in the form of heat due to viscous effects, thereby significantly raising the temperature of the aircraft surface. With increasing velocity (and Mach number), the kinetic energy of the air increases, making dissipative heat transfer more of a limiting factor, to the point where protruding surfaces (such as control surfaces required for steering) are extremely susceptible to thermal failure. As a result, hypersonic vehicles tend to have a more streamlined appearance, such as the space shuttle, which is a atmospheric re-entry vehicle. Besides thermal concerns, hypersonic vehicles require sophisticated propulsion systems and must operate at very high altitudes in order to avoid the higher air densities that exist near sea level. A higher air density corresponds to more molecules per unit volume, leading to increased drag during flight.[3] Therefore, it becomes prohibitive to achieve hypersonic flight except in rarefied regions. It now becomes more obvious why hypersonics research is very difficult and expensive to perform.

The most common way to avoid the high cost of experimental hypersonics work is to model such flows using computational codes. Computational Fluid Dynamics (CFD) codes allow continuum flows to be analyzed using the Euler and Navier-Stokes (NS) equations. As will be explained in later sections, the Euler and NS equations are not capable of accurately describing nonequilibrium flows. In fact, the Euler equations assume the flow is at equilibrium, while the NS equations assume only small deviations from equilibrium. Also, the Euler and NS equations are derived assuming that the flow is a continuous mass of fluid (continuum), which can no longer be assumed at low densities (rarefied). Therefore, CFD codes breakdown in both nonequilibrium and rarefied flows. Kinetic methods, however, make no assumptions

---

[3]The term molecule here refers to both monatomic and polyatomic particles. This usage will be followed throughout the rest of this work.

about density, but rather about how the separate molecules interact. These methods are commonly derived from kinetic theory, starting at the molecular level with the goal of describing macroscopic properties (such as density, pressure, temperature, and viscosity) with molecular interactions. Whether statistically or deterministically based, kinetic methods usually describe the flow with distribution functions, such as the velocity distribution function (VDF). The VDF describes the likelihood that any molecule in that region will have a given three-dimensional velocity. Alternately, the VDF can be seen as the *actual* distribution of velocities over all the molecules in a given region. The former statistical interpretation can be applied at any *point*, while the latter can only be applied over a *region* small enough when compared with the entire flow, but large enough that it contains enough molecules that the VDF is a continuous function. The Boltzmann equation, as will be seen later, is a governing equation for the VDF, and describes its evolution in time, physical space, and velocity space, due to intermolecular collisions. Even though the Boltzmann equation has its limitations (e.g. only considers bimolecular collisions), it has been found to be very useful, especially with modern computational capabilities.

Many flows considered in aerodynamics are in a state of equilibrium, meaning that macroscopic flow properties do not change over time. However, there are instances when significant nonequilibrium effects come into play. For example, consider a chemical process that involves chemical nonequilibrium. The original chemical composition begins at some initial state (usually at equilibrium), then a chemical reaction occurs during which the molecules are in a state of change (nonequilibrium), and finally the chemical composition arrives at (or relaxes to) a final state (again at equilibrium). Thus, nonequilibrium is the process by which a system changes from one state of equilibrium to another state of equilibrium. But there are more types of nonequilibrium than just chemical. A flow may be in chemical (to include dissociative, recombinative, and ionization), thermal, translational, rotational, vibrational, electronic, and/or radiative nonequilibrium.

The translational energy of a molecule is directly related to its velocity. This energy is transferred from one molecule to another through a molecular collision. It only takes a handful of collisions for a molecule's translational energy to equilibrate with that of its neighbors, so translational nonequilibrium is usually a short-lived process (except for the case of very low-density flows). A measure of how far apart molecules are in space is the mean free path λ (m), defined as the average distance a molecule can travel before it will collide with another molecule. Translational nonequilibrium can therefore be studied in flows with length scales on the order of the mean free path, such as shock waves or low-density (or rarefied) flows.[4]

A polyatomic molecule has some amount of rotation associated with it, leading to its rotational energy. Various models are available to describe how a molecule rotates, but for this work it is assumed that diatomic Nitrogen can be modeled as two Nitrogen atoms attached by a rigid connector.[5] Therefore, N_2 has two degrees of rotational freedom, meaning that its rotational energy is due to rotation about only two orthogonal axes (no energy is associated with rotation about the axis which passes through both atoms). Similar to translational energy, it only takes on the order of 10 molecular collisions to reach rotational equilibrium. Most aerospace applications in polyatomic flows will involve rotational energy since rotational levels begin to be excited at a temperature of about 2 K.[6] It has been observed that molecular rotation causes a centrifugal force that can decrease the energy required for dissociation.[7]

Vibrational and electronic energy, dissociation, and ionization will not be important in this study, but are interesting nonetheless. Vibrational energy is a diatomic or polyatomic phenomenon. For N_2, the atoms are separated by some link, and they tend to vibrate with some energy. Vibrational equilibrium requires many more molecular collisions than translational and rotational equilibrium (about 25 trillion collisions at room temperature). However, vibrational excitation for N_2 only becomes important

---

[4]Strong shocks have a thickness of only a few mean free paths.
[5]This model is called the rigid rotator model.
[6]For N_2, the characteristic temperature for rotation is 2.9 K
[7]Dissociation occurs when an atom breaks free from the bonds that hold it to the other atom(s).

at about 3,390 K. Electronic energy only contributes a small amount to the overall energy in practical applications, and is usually neglected, as is the case here. Dissociation and ionization are only encountered in very high-temperature flows, since in N_2 they become important at about 113,000 K and 181,000 K, respectively.

Continuum flows, as described by the NS equations, only experience small deviations from equilibrium.[8] Efforts have been made to therefore distinguish between continuum and non-continuum (or rarefied) flows, and are in fact still underway with recent interest in hybrid codes. One common measure of whether a flow is continuum or rarefied is the Knudsen number Kn, defined as the ratio of the mean free path λ to a characteristic length of the flow L (m):

$$Kn = \frac{\lambda}{L} \tag{1}$$

A low Knudsen number corresponds to continuum flow, while a large value corresponds to rarefied flow, and a *very* large value indicates free molecular flow. The choice of L is somewhat arbitrary, and really depends on the problem at hand. For example, flow over an aircraft wing might use the mean aerodynamic chord for L (small Kn), while the boundary-layer flow over the same wing could use for L the boundary layer height $\delta_{99\%}$ (intermediate Kn), and the flow through the shock standing off from the nose would use the shock thickness for L (large Kn). On the other hand, λ is dependent mainly on the density of the flow. The mean free path would be much larger at higher altitudes (high Kn, low density) than at sea level (low Kn, high density).

A notional categorization of flows based on the local Knudsen number is shown in Figure 1. Continuum regions roughly have $Kn \leq 0.01$, near-continuum regions span $0.01 < Kn \leq 0.1$ (the continuum assumptions begin to break down), rarefied regions typically have values of $0.1 < Kn \leq 10$ (the continuum assumptions are no

---

[8]Attempts are still being made to extend the range of applicability of continuum solvers. For example, Claycomb studied how including bulk viscosity into a NS solver can extend the effectiveness of a continuum solver into regimes with high degrees of nonequilibrium [8].
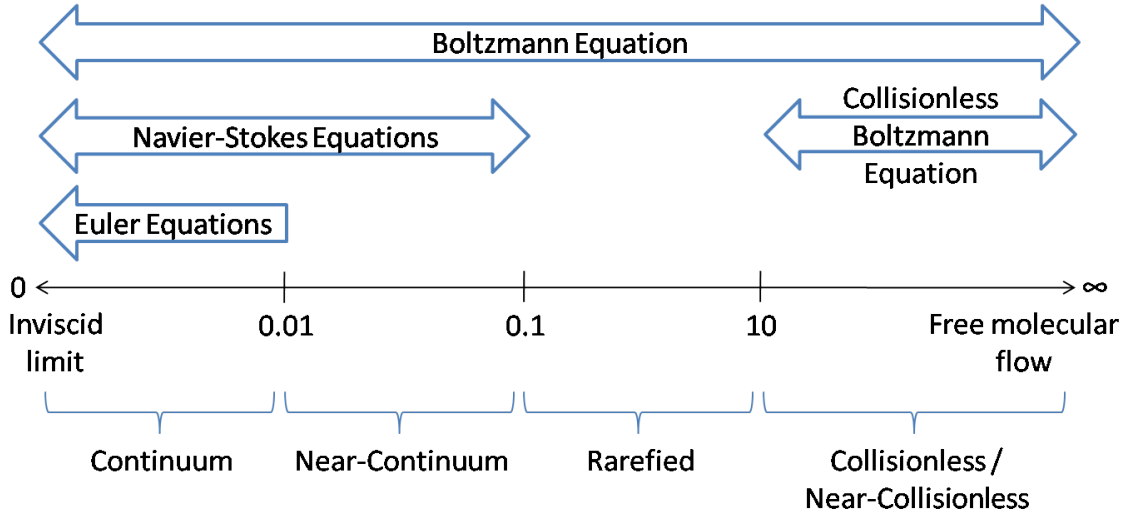
Figure 1: Notional local Knudsen number flow categories.

longer valid), and flows with $Kn > 10$ experience so few molecular collisions that they are seen as near-collisionless or collisionless.

The Knudsen number is not the only measure of continuum breakdown. As was previously discussed, continuum assumptions are closely tied to a state of equilibrium, or even near-equilibrium. Likewise, rarefied regions display a greater departure from equilibrium due to the large time factors between molecular collisions, and therefore are typically non-equilibrium flows. The study of classical thermodynamics relates the process by which one equilibrium state changes to another equilibrium state with a scalar parameter, entropy. Schrock and Carr investigated this further by looking at how a continuum breakdown parameter based on entropy could be used to better characterize continuum flow [7, 34]. One drawback of their method is that the more computationally expensive rarefied methods, such as the Direct Simulation Monte Carlo (DSMC) method, must first be used to calculate the entropy in order to determine whether the continuum assumptions hold for that cell. Kolobov et al. suggests two continuum breakdown criteria, or switching parameters for the UFS hybrid code, based on either density gradients or pressure and velocity gradients [21]. Using the correct switching parameter is important in UFS, because otherwise non-positive VDFs may be obtained, which is physically impossible [21].

Besides determining continuum and rarefied (or kinetic) domains, hybrid codes must also choose an appropriate coupling method. Three classes of coupling have been considered to date [21]. The first decomposes the physical domain into kinetic and continuum sub-domains. The second instead decomposes the velocity domain and considers separately fast and slow particles. The third calculates the VDF in all the cells and then uses that information to compute transport properties for the continuum equations. UFS takes the last approach.

There is a trade-off between efficiency and accuracy in computational modeling. Consider as an example of extreme accuracy the flow over an airfoil at sea level. Here the ambient density is relatively high, which means that molecules are spaced closely together.[9] Using classical mechanics, one could conceivably follow the velocity and position (in spite of the Heisenberg Uncertainty Principle) of every molecule. Every time a molecule collides with another (assuming a billiard-ball, or hard-sphere model), the deflection angles and momentum changes would be calculated. Of course, air is composed of many different species (e.g. O_2, N_2, etc.), which would only complicate things. The flow of such a large amount of molecules over even a simple airfoil would be prohibitively expensive to compute. Besides, how would one know the exact starting positions and velocities of every particle? In addition, the hard-sphere model of a molecule ignores all internal energies, only accounting for an effective collision diameter, molecular mass, and translational energy. Instead of the previous deterministic approach, one might take a statistical sampling of an aggregate of molecules, and approximate it as one simulated molecule (as is the case with DSMC). However, by making the problem simpler and more manageable with simulated molecules, one has also lost a measure of accuracy. The main point that must be determined for any given computational model is how well it balances this trade-off.

In an effort to more efficiently and/or accurately describe rarefied flows, the Air Vehicles Directorate of AFRL recently contracted the CFD Research Corporation

---

[9]It is estimated that at sea level, there are 2.5×10^{25} molecules per m^3 of air, and λ is on the order of 0.1 μm.

(CFDRC) to create a kinetic-based hybrid code called the Unified Flow Solver (UFS) [20–22]. UFS is meant to be more efficient than a DSMC code for near-continuum and transition flows, and more accurate than Euler and NS solvers for transition and rarefied flows. A hybrid code is one that can solve rarefied and continuum flows, as well as transition flows (flows that have both rarefied and continuum regions such as the hypersonic flow over a cylinder). UFS uses the Boltzmann equation to solve for the VDF in each cell, and then calculates the macroscopic flow quantities from the VDF. Hybrid solvers continue to be an active research area, with more developments expected in the future.

This work has two parts. The first studies one-dimensional shock waves in Argon and Nitrogen (N_2) using UFS and comparing the results to the experimental data from Alsmeyer and numerical simulations using Bird's DSMC method [3]. Shock structure provides a useful test case for any new code, such as UFS, since it involves translational, rotational, and vibrational molecular nonequilibrium.

The second part of this study examines how an entropy spot (i.e. a temperature or a density spot) affects a two-dimensional shock in Argon using one of UFS's kinetic solvers for $Kn = 0.01$, 0.1, and 1.0 at Mach 2.0. There are three basic modes of disturbance in a gas (acoustic or pressure, vortical, and entropy), and any disturbance can be decomposed into a linear combination of these three modes [12]. Initially, studies were focused on noise generation (acoustic effects) due to turbulence traveling through a shock, using a small vortex perturbation in the flow to simulate localized turbulence [5, 15, 25, 26, 28, 31, 41]. More recently, articles by Duck et al. have extended the freestream disturbance analysis to include acoustic, vorticity, and entropy waves, showing analytically that when any one of these disturbances travels through an oblique shock, all three modes are created downstream [9, 10]. As discussed by Fabre et al., a cylindrical entropy spot can be decomposed using Fourier synthesis into plane entropy waves arranged with different orientations [11]. Thus, an entropy spot traveling through a normal shock will excite acoustic, vortical, and entropy disturbances downstream of the shock.

Hussaini and Erlebacher provide multiple reasons why entropy-shock interactions are important in aerospace applications, such as turbulence amplification in shock-turbulent boundary layer interactions, density fluctuations in supersonic wake-shock interactions, noise generation in hot rocket exhausts with oblique shock waves, and enhanced mixing caused by shock interactions in the combustor of a scramjet engine with hot and cold flows (oxidant and fuel) [16]. Numerical studies have been performed on entropy-shock interactions using two-dimensional Euler schemes [11–13,16]. However, no results have yet been presented with either the NS equations or with a kinetic solver. This work hopes to begin such a study.

II. Related Theory

Since UFS is heavily based on kinetic theory and the Boltzmann equation, this chapter briefly introduces the kinetic theory of gases, the Boltzmann equation, and a useful approximation to the Boltzmann equation. Also, the numerical schemes for the solvers implemented in UFS are presented here to give the reader a better understanding of how UFS performs its calculations.

2.1   Kinetic Theory of Gases

Kinetic theory seeks to explain macroscopic flow phenomena by investigating molecular interactions. For example, the transport phenomena of viscosity, heat conduction, and diffusion can be explained by the molecular transport of momentum, energy, and mass, respectively.

To begin with, assume a molecule can be modeled as a rigid sphere with no internal structure. The only physical characteristics of the molecule are then an effective diameter and a mass. This molecular model is, of course, a simplification. In reality, electron clouds are not always spherically symmetric, and polyatomic molecules may have an intricate structure with rotational, vibrational, and electronic energies. However, the rigid sphere model is a good starting point. Normally, molecules interact not just during physical "contact" because they have an intermolecular force that is a function of their distance from each other. Strangely, this force is repulsive at short distances, but attractive at large distances, while the more familiar gravitational force is solely attractive. The rigid sphere model instead assumes that at some effective diameter, there is an infinite repulsive force, and everywhere else the intermolecular force is zero. The dynamics of rigid sphere molecules, therefore, act as moving billiard balls on a table, knocking each other around only as they collide. The intermolecular force can be modified beyond this simplification within kinetic theory, as will be discussed.

Each of the molecules has a translational (or kinetic) energy, which is dependent on the macroscopic temperature. However, every molecule does not travel in space

with the same speed, nor in the same direction. Some molecules have a higher velocity than the mean velocity, while some have a lower velocity than the average. Over time, a certain molecule's velocity will change due to collisions, but the average velocity of all the molecules per unit volume will remain the same when the system is in equilibrium. Because there are so many molecules per unit volume, the distribution of velocities over a unit volume in velocity space can be represented by the VDF. Velocity space has as its axes the velocities in the coordinate directions (C_1, C_2, and C_3), instead of the spatial axes (x, y, and z). Therefore, regardless of where a molecule lies in physical space, its point in velocity space corresponds to its u-, v-, and w-components of velocity. The VDF is a normalized distribution function, meaning that the volume under its curve is equal to unity:

$$\int_{-\infty}^{\infty} f(C_i)dC_i = 1 \tag{2}$$

where f is the normalized VDF, C_i is the molecular velocity vector (m/s), and $dC_i = dC_1\, dC_2\, dC_3$ is an element in velocity space (m^3). Also, the average of any quantity Q that is also a function of velocity, can be calculated from

$$\bar{Q}(C_i) = \int_{-\infty}^{\infty} Q(C_i)f(C_i)dC_i \tag{3}$$

For example, the average velocity in the x-direction $\bar{C}_1$ is

$$\bar{C}_1 = \int_{-\infty}^{\infty} C_1 f(C_i)dC_i \tag{4}$$

Equations (2) and (3) are the zeroth and first moments of the VDF, respectively, where the nth moment of the VDF M_n is defined as

$$M_n = \int_{-\infty}^{\infty} Q(C_i)f(C_i)dC_i \tag{5}$$

11

The VDF for a gas at equilibrium has been well established, and was first published by Maxwell in 1860. It bears his name as the Maxwellian distribution:

$$f^{eq} = \left(\frac{m}{2\pi kT}\right)^{3/2} \exp\left[-\frac{m}{2kT}(C_1^2 + C_2^2 + C_3^2)\right] \tag{6}$$

where m is the molecular mass (kg), k is the Boltzmann constant (1.38×10^{-23} kg $\cdot$ m^2/s$^2 \cdot$ K), and T is the temperature (K). Following the development by Vincenti and Kruger, define a new function Φ [37]:

$$\Phi(C_1) = \left(\frac{m}{2\pi kT}\right)^{1/2} \exp\left[-\frac{m}{2kT}C_1^2\right] \tag{7}$$

and then

$$f^{eq}(C_i) = \Phi(C_1)\Phi(C_2)\Phi(C_3) \tag{8}$$

In other words, each of the velocity component distribution functions $\Phi(C_i)$ is statistically independent from the others. The Maxwellian distribution is shown in Figure 2 with an average molecular velocity of zero. For equilibrium, the distribution is symmetric about its mean. Also, for all VDFs, the macroscopic velocity corresponds to the average velocity. The above analysis uses the thermal velocity, C_i (m/s):

$$C_i \equiv c_i - \bar{c}_i \tag{9}$$

where c_i is the molecular velocity (m/s) as seen from a stationary observer, and $\bar{c}_i$ is the average molecular (or macroscopic gas) velocity (m/s) also observed by a stationary observer. f^{eq} can then be written as

$$f^{eq} = \left(\frac{m}{2\pi kT}\right)^{3/2} \exp\left[-\frac{m}{2kT}(|c_i - \bar{c}_i|)^2\right] \tag{10}$$

since $C^2 = C_1^2 + C_2^2 + C_3^2 = (|c_i - \bar{c}_i|)^2$. So, Figure 2 is actually showing the thermal velocity distribution. To include the macroscopic velocity, the distribution
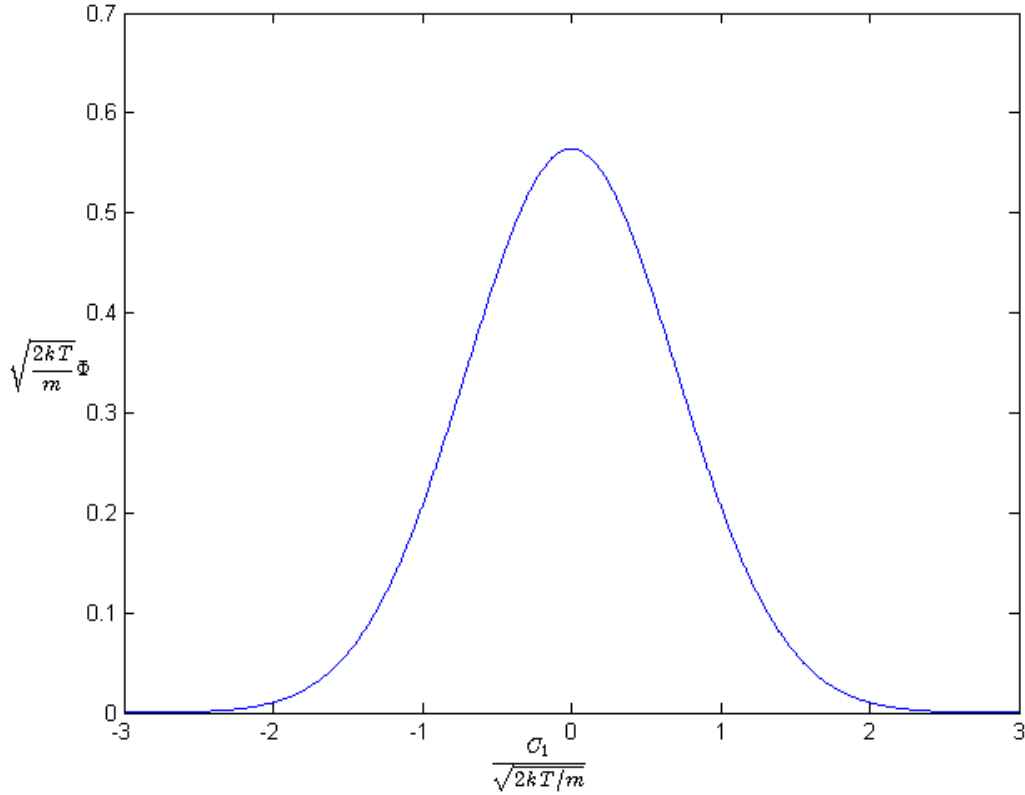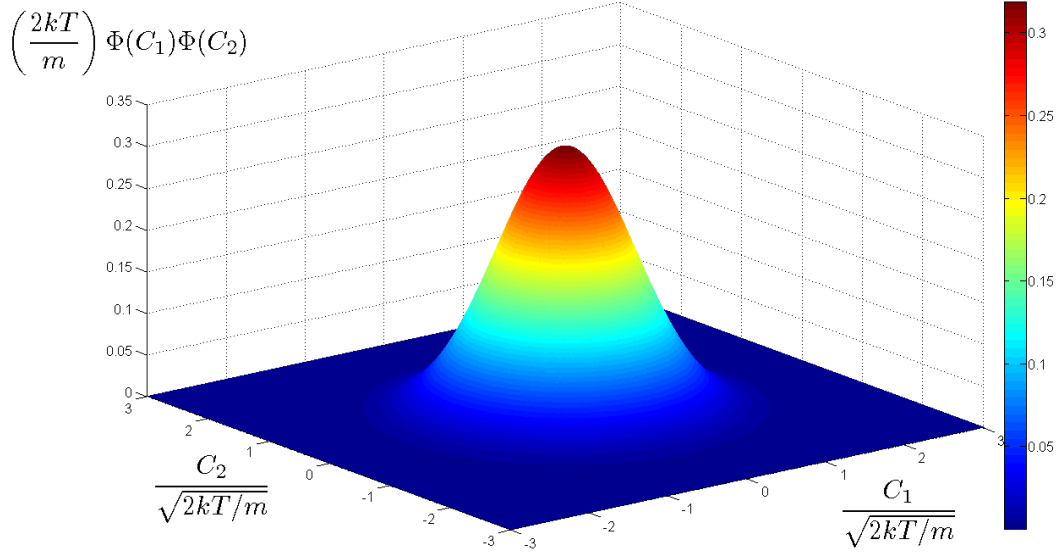
12

Figure 2: Non-dimensional Maxwellian distribution function for only one component of the thermal velocity (centered on the average flow velocity).

in Figure 2 needs only to be shifted on the horizontal axis. As noted by Vincenti and Kruger, in a dimensional plot of Φ versus C_1, increasing only the temperature widens the curve and lowers the maximum, while increasing only the molecular mass has just the opposite effect [37]. Since the full VDF is actually in three-dimensional velocity space, it is difficult to visualize. However, Figure 3 gives a two-dimensional representation of the equilibrium VDF.

The VDF is also used to calculate other macroscopic flow variables such as ρ (kg/m^3), velocity $\bar{c}_i$, temperature T, pressure p (N/m^2), shear stress τ_{ij} (N/m^2), and heat flux q_i (W/m^2), using its moments [36]:

13

Figure 3: Non-dimensional Maxwellian distribution function for two components of the thermal velocity (centered on the average flow velocity).

$$\rho = m \int_{-\infty}^{\infty} n f(c_i) dc_i \tag{11}$$

$$\bar{c}_i = \int_{-\infty}^{\infty} c_i f(c_i) dc_i \tag{12}$$

$$T = \frac{1}{3R} \int_{-\infty}^{\infty} (c_i - \bar{c}_i)^2 f(c_i) dc_i \tag{13}$$

$$p = \frac{1}{3}\rho \int_{-\infty}^{\infty} (c_i - \bar{c}_i)^2 f(c_i) dc_i \tag{14}$$

$$\tau_{ij} = \rho \int_{-\infty}^{\infty} (c_i - \bar{c}_i)(c_j - \bar{c}_j) f(c_i) dc_i \tag{15}$$

$$q_i = \frac{1}{2}\rho \int_{-\infty}^{\infty} (c_i - \bar{c}_i)(c_j - \bar{c}_j)^2 f(c_i) dc_i \tag{16}$$

where R is the specific gas constant (J/kg·K), and n is the number density (or number of molecules per unit volume, $1/m^3$).[1]

---

[1]It is interesting to note that temperature and pressure are directly proportional to the variance of the VDF $\int (c_i - \bar{c}_i)^2 f(c_i) dc_i$.

14

Chapman and Enskog independently analyzed small departures from nonequilibrium using an expansion of f about f^{eq}:

$$f = f^{eq}(1 + \Phi_1 + \Phi_2 + \Phi_3 + \Phi_4 + \cdots) \tag{17}$$

where $\Phi = \Phi(Kn)$, and Φ_n denote higher-order terms. It can be shown that when only the zeroth-order term is considered (the first term in the expansion), the Euler equations are realized, and when first-order terms are included, the NS equations are achieved. Higher-order terms have been included to develop the Burnett (second-order terms), the Super-Burnett (third-order terms), and the Super-Super-Burnett (fourth-order terms) equations, even though their usefulness seems to be limited.[2] The Chapman-Enskog expansion provides a useful interpretation of the Euler and NS equations. The Euler equations, because they only include the zeroth-order term, assume the flow is always at equilibrium, showing that viscosity and heat fluxes are nonequilibrium phenomena. The NS equations, because they include at most the first-order terms, assume the flow only experiences small departures from nonequilibrium. Therefore, continuum relations become invalid for flows that depart significantly from nonequilibrium.

Since it is very expensive computationally to follow every particle in a flow, it would be useful to solve for the VDF directly using some governing equation. The Boltzmann equation is such a governing equation for the VDF, describing how the VDF evolves in space and time. The number of molecules of class c_i (meaning with velocity c_i) in a physical space volume element $dV_x \equiv dx\,dy\,dz$ (m^3) and in a velocity space volume element $dV_c \equiv dc_1\,dc_2\,dc_3$ (m^3/s^3) is $nf(c_i)dV_xdV_c$, where n is the number of molecules per unit physical volume (1/m^3). The number of molecules in

---

[2]For a study on one-dimensional shock structure in a monatomic gas using the Super-Burnett and Super-Super-Burnett equations, see [35].

these volume elements, over time, is then

$$\frac{\partial}{\partial t}[nf(c_i)] \, dV_x \, dV_c \tag{18}$$

which can only be a result of convection of molecules in physical space, convection of molecules in velocity space, or collisions within dV_x which deplete or increase the number of molecules of class c_i. Considering all six sides of the volume element dV_x, the convection in physical space is modeled as

$$-c_j \frac{\partial}{\partial x_j}[nf(c_i)] \, dV_x \, dV_c \tag{19}$$

The convection in velocity space would be caused by an acceleration F_i (m/s^2) due to some external force, such as gravity or an electromagnetic field:

$$-\frac{\partial}{\partial c_j}[F_j nf(c_i)] \, dV_x \, dV_c \tag{20}$$

The general term

$$\left\{ \frac{\partial}{\partial t}[nf(c_i)] \right\}_{coll} dV_x \, dV_c \tag{21}$$

is used to describe how molecules of class c_i increase due to collisions. Combining these terms and dividing by $dV_x \, dV_c$, the full Boltzmann equation is

$$\frac{\partial}{\partial t}[nf(c_i)] + c_j \frac{\partial}{\partial x_j}[nf(c_i)] + \frac{\partial}{\partial c_j}[F_j nf(c_i)] = \left\{ \frac{\partial}{\partial t}[nf(c_i)] \right\}_{coll} \tag{22}$$

The term on the right-hand side is called the collision term, or the collision integral, because its direct calculation involves multi-dimensional integration. Vincenti and Kruger develop the collision integral for hard-sphere molecules (with a spherical

16

intermolecular potential), given as [37]

$$\left\{\frac{\partial}{\partial t}[nf(c_i)]\right\}_{coll} = \int_{-\infty}^{\infty}\int_{0}^{2\pi}\int_{0}^{\pi/2} n^2\left[f(c_i')f(\zeta_i') - f(c_i)f(\zeta_i)\right] g\, d^2\, \sin\psi\, \cos\psi\, d\psi\, d\epsilon\, dV_\zeta$$

(23)

where c_i and ζ_i are the pre-collisional velocities and c_i' and ζ_i' are the post-collisional velocities of the two molecules (m/s), $g = |\zeta_i - c_i|$ is the relative molecular speed (m/s), d is the diameter of the molecules (m), $d^2\sin\psi\cos\psi d\psi d\epsilon$ is the collisional differential cross-section on a sphere, and dV_ζ is the volume element $d\zeta_1\, d\zeta_2\, d\zeta_3$ in velocity space. The first term in the collision integral represents inverse collisions which replenish the number of molecules of class c_i, while the second term represents collisions which deplete the number of molecules of class c_i.[3]

A couple of observations can be made at this point about the Boltzmann equation. The first observation is that the Boltzmann equation is an integro-differential equation, meaning that the VDF is the argument of both integrals and differentials, making it very difficult to evaluate. The second is that the Boltzmann equation assumes that only bimolecular collisions, or collisions involving only two molecules, occur. Collisions involving more than two molecules are more likely to occur when the density is high. However, the densities encountered in this work are low enough that this assumption applies.

The Boltzmann equation can be arrived at from the more general Liouville equation, which is in $6N$-dimensions describing how every possible microstate (defined by the position and momentum of every particle) is tracked in phase space (the space of *all* states at which the system can exist).[4] The Boltzmann equation can be rigorously derived from the Liouville equation by only considering the one-particle distribution function f and integrating over all dimensions except for c_i and x_i. An in-depth

---

[3]For identical incidence angles, the velocities after a deplenishing collision are equal to c_i and ζ_i, while the the velocities after a replenishing inverse collision are equal to c_i and ζ_i.

[4]Here, N denotes the number of molecules.

discussion of this subject is beyond the scope of this work, and the reader is referred to the book by Harris for a more complete introduction [14].

Even though the Boltzmann equation has been around for many years, an analytic solution has not been found. In an attempt to avoid the costly calculation of the collision integral, approximate models to the Boltzmann equation have been proposed. One such model was developed by Bhatnagar, Gross, and Krook, called the Bhatnagar-Gross-Krook (BGK) collision model [37]. The BGK model, even though it involves a simplification of the collision term, tries to retain some features of the same. The collision term is replaced by

$$\left\{ \frac{\partial}{\partial t}[nf(c_i)] \right\}_{coll} = n\nu(f^{eq} - f) \tag{24}$$

where ν is a collision frequency (Hz, or 1/s), f^{eq} is the equilibrium (or Maxwellian) distribution, and f is the variable VDF. The full BGK model is therefore

$$\frac{\partial}{\partial t}[nf(c_i)] + c_j\frac{\partial}{\partial x_j}[nf(c_i)] + \frac{\partial}{\partial c_j}[F_j nf(c_i)] = n\nu(f^{eq} - f) \tag{25}$$

Since ν is a collision frequency, it could also be written as $1/\tau_\nu$, where τ_ν is a local relaxation time (s). Therefore, the BGK collision term takes on the same form as that used in the vibrational relaxation equation. In light of this relationship, the BGK model essentially describes how a gas in nonequilibrium relaxes (or equilibrates) to a state of equilibrium. So, one of the drawbacks of the BGK model is that it loses accuracy or validity as the departure from nonequilibrium increases.[5] Vincenti and Kruger also note that since f^{eq} is a function of $\bar{c}_i$ and T, and since $\bar{c}_i$ and T are calculated as moments of the VDF (see Equations (12) and (13)), the BGK equation is still a nonlinear integro-differential equation [37].[6]

---

[5]Xu and Guo extended the BGK model further into the nonequilibrium regime by replacing the one-stage BGK collision model with a two-stage model [40].

[6]See Equation (10).

Another aspect of the molecular model that should be considered is the intermolecular potential. Molecules far apart tend to weakly attract one another, whereas molecules close in proximity tend to strongly repel one another. The Hard Sphere (HS) model, because it does not account for any other interaction besides collisions, assumes only an infinitely large repulsive force during a collision. The Sutherland model, on the other hand, also allows for an attractive force that decreases with distance. When solving the Boltzmann equation, one usually must define which intermolecular potential model one is using. With the BGK model, however, since the collision integral is replaced entirely, no explicit potential model is used. Rather, a certain collision model is specified in the calculation of ν (this study uses the HS collision model).

2.2   UFS Methods

UFS is built on the Gerris code [2]. Gerris is an open-source code which was initially released in 2005 and is supported by New Zealand's NIWA (National Institute of Water and Atmospheric research). It is a time-dependent, second-order (in time and space), finite-volume solver for incompressible flows, with the option of using either an Euler or a NS scheme, and is capable of parallel computing using the MPI (Message-Passing Interface) library. It uses Cartesian quadtree (two-dimensional) or octree (three-dimensional) grids, meaning that all cells are either squares or cubes, whose dimensions only differ by some factor of two. The grid structure will be discussed more in Chapter III in reference to the particular grids used in this study.

UFS utilizes both continuum and kinetic solvers when computing flow parameters. The user can specify which solvers to use, and where in the domain they should be called. The kinetic solvers are either approximations of the Boltzmann equation (such as the BGK model) or DNS (Direct Numerical Simulation) of the collision integral using some intermolecular force model. As of 2006, four intermolecular force models have been included in UFS, namely the HS model, the inverse power repulsive potential, the Lennard-Jones potential, and the Coulomb potential [21].

19

As explained by Kolobov et al., the Boltzmann equation as Equation (22) can also be framed in the following form when neglecting external forces [21]:

$$\frac{\partial f}{\partial t} + \nabla_{\boldsymbol{r}} \cdot (\boldsymbol{\xi} f) = I(f, f) \tag{26}$$

where $\boldsymbol{r}$ is a position vector in physical space (m), $\boldsymbol{\xi}$ is the velocity vector (m/s), and $I(f, f)$ is the collision integral. In order to solve Equation (26) numerically, a Cartesian mesh is created in velocity space with nodes $\boldsymbol{\xi_i}$ and cell size $\boldsymbol{\Delta\xi}$ (m/s).[7] It is claimed that by using this mesh, Equation (26) is reduced to a system of linear equations (hyperbolic) in physical space with the nonlinear source term

$$\frac{\partial f_i}{\partial t} + \nabla_{\boldsymbol{r}} \cdot (\boldsymbol{\xi_i} f_i) = I(f_i, f_i) \tag{27}$$

where the subscript i indicates that the parameter is evaluated at nodes i. Since UFS is built on the Gerris solver, which utilizes only Cartesian grids in physical space, the computational grid in physical space in UFS is also Cartesian. Equation (27) is solved in two stages—collisionless flow and relaxation, divided by an intermediate time stage.

For the collisionless flow stage, the collision integral is assumed to be zero, and an explicit finite volume scheme is used:

$$V\frac{f_{ij}^{*k} - f_{ij}^{k-1}}{\Delta t} + \sum_{\text{face}} (\boldsymbol{\xi}_i \cdot \boldsymbol{n})_{\text{face}} \, f_{i,\text{face}}^{k-1} \, S_{\text{face}} = 0 \tag{28}$$

where j is the cell number in physical space, k is the time index, $*$ indicates an intermediate time level, $\boldsymbol{n}$ is the unit outward normal vector to the cell face, V is the cell volume (m³), S_{face} is the face surface area (m²), and $f_{i,\text{face}}^{k-1}$ is the value of the VDF on the cell face. To calculate $f_{i,\text{face}}^{k-1}$, interpolation schemes are used (either first- or second-order), with three options for the second-order limiter: none, minmod, or

---

[7]In future work, CFDRC hopes to include automatic mesh refinement in velocity space, which would save computational expense as well as make velocity-space grid independence studies simpler.

van Leer. The minmod limiter, which is the most conservative of the second-order limiters, is used in this study.

For the relaxation stage,

$$\frac{f_{ij}^k - f_{ij}^{*k}}{\Delta t} = -\nu_{ij}^{*k} f_{ij}^{*k} + \Phi_{ij}^{*k} \tag{29}$$

where ν is the collision frequency (how often molecules in class $\boldsymbol{\xi}$ are depleted) and Φ is the inverse collision integral. Similar to the BGK model, UFS replaces here the complex collision integral with two terms ($-\nu f$ and Φ), illustrating again that the BGK model describes how the distribution function relaxes to equilibrium.

The continuum solvers are also based on the Boltzmann equation because macroscopic flow parameters can be obtained through the moments of the VDF. Also, coupling of the continuum and kinetic solvers is easier when they are all based on the Boltzmann equation. Again, Kolobov et al. present the following material concerning the Euler and NS solvers, which is included here for completeness [21].

The Euler equations can be presented in the form

$$\frac{\partial \boldsymbol{Y}}{\partial t} + \frac{\partial \boldsymbol{F}}{\partial x} + \frac{\partial \boldsymbol{G}}{\partial y} + \frac{\partial \boldsymbol{H}}{\partial z} = 0 \tag{30}$$

where

$$\boldsymbol{Y} = [\rho, \ \rho u, \ \rho v, \ \rho w, \ E] \tag{31}$$

$$\boldsymbol{F} = [\rho u, \ p/2 + \rho u^2, \ \rho uv, \ \rho uw, \ u(E+p)] \tag{32}$$

$$\boldsymbol{G} = [\rho v, \ \rho uv, \ p/2 + \rho v^2, \ \rho vw, \ v(E+p)] \tag{33}$$

$$\boldsymbol{H} = [\rho w, \ \rho uw, \ \rho vw, \ p/2 + \rho w^2, \ w(E+p)] \tag{34}$$

and ρ is the density (defined as $\rho = mn$), u, v, and w are the flow velocities in the x-, y-, and z-directions (m/s), respectively, E is the energy (J):

$$E = \frac{3}{2}\rho T + \rho(u^2 + v^2 + w^2) \tag{35}$$

T is the temperature, and $p = nkT$ is the pressure. Discretizing Equation (30) with an explicit finite volume scheme, and moving spatial derivatives to the right-hand side,

$$\frac{\boldsymbol{Y}_{ijk}^{n+1} - \boldsymbol{Y}_{ijk}^{n}}{\Delta t} = \\ -\left(\frac{\boldsymbol{F}_{i+1/2,j,k}^{n} - \boldsymbol{F}_{i-1/2,j,k}^{n}}{\Delta x} + \frac{\boldsymbol{G}_{i,j+1/2,k}^{n} - \boldsymbol{G}_{i,j-1/2,k}^{n}}{\Delta y} + \frac{\boldsymbol{H}_{i,j,k+1/2}^{n} - \boldsymbol{H}_{i,j,k-1/2}^{n}}{\Delta z} \right) \tag{36}$$

where n denotes the time step, i, j, and k denote the cell nodes in physical space for the x-, y-, and z-directions, $\boldsymbol{Y}_{ijk}^{n}$ is the cell-averaged value at time step n, and $\boldsymbol{F}_{i+1/2,j,k}^{n}$, $\boldsymbol{G}_{i,j+1/2,k}^{n}$, and $\boldsymbol{H}_{i,j,k+1/2}^{n}$ indicate the fluxes on the cell faces along the x-, y-, and z-directions, respectively. The fluxes are calculated using moments of the distribution function:

$$\boldsymbol{F}_{i\pm1/2,j,k} = \frac{1}{\Delta t} \int_{t^n}^{t^{n+1}} \int_{\mathbb{R}^3} \boldsymbol{\psi}\xi_x f(x_{i\pm1/2},\, y_j,\, z_k,\, t,\, \boldsymbol{\xi})\, d\boldsymbol{\xi}\, dt \tag{37}$$

$$\boldsymbol{G}_{i,j\pm1/2,k} = \frac{1}{\Delta t} \int_{t^n}^{t^{n+1}} \int_{\mathbb{R}^3} \boldsymbol{\psi}\xi_y f(x_i,\, y_{j\pm1/2},\, z_k,\, t,\, \boldsymbol{\xi})\, d\boldsymbol{\xi}\, dt \tag{38}$$

$$\boldsymbol{H}_{i,j,k\pm1/2} = \frac{1}{\Delta t} \int_{t^n}^{t^{n+1}} \int_{\mathbb{R}^3} \boldsymbol{\psi}\xi_z f(x_i,\, y_j,\, z_{k\pm1/2},\, t,\, \boldsymbol{\xi})\, d\boldsymbol{\xi}\, dt \tag{39}$$

where $\mathbb{R}^3$ indicates that the integral is over all real values in velocity space, and $\boldsymbol{\psi}$ signifies the collisional invariants, given as $\boldsymbol{\psi}(\boldsymbol{\xi}) = [1,\, \boldsymbol{\xi},\, \xi^2]$. The collisional

invariants are so named because they have the property that[8]

$$\int_{\mathbb{R}^3} \psi I(f, f) d\boldsymbol{\xi} = 0 \tag{40}$$

The VDF at the cell faces is calculated as

$$f(x_{i+1/2}, y_j, z_k, t, \boldsymbol{\xi}) = H[\xi_x] f_l^{eq} + (1 - H[\xi_x]) f_r^{eq} \tag{41}$$

where f_l^{eq} and f_r^{eq} are the equilibrium VDFs on the cell's left and right faces, respectively:

$$f_l^{eq} = \frac{\rho_{i-1/2}}{\left(\pi T_{i-1/2}^n\right)^{3/2}} \exp\left[-\frac{(\xi_x - u_{i-1/2,j,k})^2 + (\xi_y - v_{i-1/2,j,k})^2 + (\xi_z - w_{i-1/2,j,k})^2}{T_{i-1/2}^n} \right]$$
$$\tag{42}$$

$$f_r^{eq} = \frac{\rho_{i+1/2}}{\left(\pi T_{i+1/2}^n\right)^{3/2}} \exp\left[-\frac{(\xi_x - u_{i+1/2,j,k})^2 + (\xi_y - v_{i+1/2,j,k})^2 + (\xi_z - w_{i+1/2,j,k})^2}{T_{i+1/2}^n} \right]$$
$$\tag{43}$$

and $H[\xi]$ is the Heaviside step function:

$$H[\xi] = \begin{cases} 1, & \xi > 0 \\ 0, & \xi \leq 0 \end{cases} \tag{44}$$

Hence, the Euler scheme uses only Maxwellian VDFs, which is consistent with the zeroth-order Chapman-Enskog expansion. If a Boltzmann solver is being used in a neighboring cell, then the parameters required for the calculation of $f_{l,r}^{eq}$ in Equations (42) and (43) are found from moments of the VDF in the neighboring cell. Similarly, a Boltzmann cell would assume a Maxwellian VDF in a neighboring Euler cell. The first-order Euler scheme uses only a two-cell stencil ($x_{i,j}$ and $x_{i+1,j}$, or $x_{i-1,j}$

---

[8]For a more detailed description of the collisional invariants, the reader is referred to Sone's book on kinetic theory [36].

23

and $x_{i,j}$), while the second-order discretization uses a three-cell stencil ($x_{i-1,j}$, $x_{i,j}$, and $x_{i+1,j}$) with one of the three available limiters.

The kinetic NS solver is also based on the solution of the Boltzmann equation, although in a somewhat different fashion [39]. It is taken from the BGK model:

$$\frac{\partial f}{\partial t} + \nabla_r \cdot (\boldsymbol{\xi} f) = \frac{f^{eq} - f}{\tau} \tag{45}$$

where τ is the intercollision relaxation time (s) defined as $\tau = \mu/p$, and μ is the dynamic viscosity (N·s/m^2). A directional splitting method is used to reduce these multi-dimensional equations to a set of one-dimensional equations, and then solved analytically [39]. For a one-dimensional case, the VDF is solved to be

$$f(x, \boldsymbol{\xi}, t) = e^{-t/\tau} f_0(x - \xi_x t, \boldsymbol{\xi}, 0) + \frac{1}{\tau} \int_0^t f^{eq}(x_l, \boldsymbol{\xi}, t_l) e^{-(t-t_l)/\tau} dt_l \tag{46}$$

where t_l is a dummy integration variable for time (s), x_l is the trajectory of the particles (m), calculated as $x_l = x - u(t - t_l)$, and the functional dependencies on y and z have been omitted. The VDF is calculated for each cell i with faces $i + 1/2$ and $i - 1/2$, with the VDF at some initial moment f_0:

$$f_0 = f(x, \boldsymbol{\xi}, t = 0)$$
$$= f_l^{eq}[1 + a_l x - \tau(a_l \xi_x + A_l)](1 - H[x]) + f_r^{eq}[1 + a_r x - \tau(a_r \xi_x + A_r)]H[x] \tag{47}$$

and the equilibrium VDF f^{eq} is calculated from

$$f^{eq} = f_0^{eq}[1 + (1 - H[x])\bar{a}_l x + H[x]\bar{a}_r x + At] \tag{48}$$

24

where

$$a_{l,r} = \alpha_{l,r}^1 + \alpha_{l,r}^2 \xi_x + \alpha_{l,r}^3 \xi_y + \alpha_{l,r}^4 \xi_z + \alpha_{l,r}^5 (\xi_x^2 + \xi_y^2 + \xi_z^2) \tag{49}$$

$$\bar{a}_{l,r} = \bar{\alpha}_{l,r}^1 + \bar{\alpha}_{l,r}^2 \xi_x + \bar{\alpha}_{l,r}^3 \xi_y + \bar{\alpha}_{l,r}^4 \xi_z + \bar{\alpha}_{l,r}^5 (\xi_x^2 + \xi_y^2 + \xi_z^2) \tag{50}$$

$$A_{l,r} = A_{l,r}^1 + A_{l,r}^2 \xi_x + A_{l,r}^3 \xi_y + A_{l,r}^4 \xi_z + A_{l,r}^5 (\xi_x^2 + \xi_y^2 + \xi_z^2) \tag{51}$$

$$A = A^1 + A^2 \xi_x + A^3 \xi_y + A^4 \xi_z + A^5 (\xi_x^2 + \xi_y^2 + \xi_z^2) \tag{52}$$

are polynomial functions of the local constants $\alpha_{l,r}^i$, $\bar{\alpha}_{l,r}^i$, $A_{l,r}^i$, and A^i ($i = 1, 2, 3, 4, 5$), and $f_0^{eq} = f^{eq}(x, \boldsymbol{\xi}, t = 0)$, which are all determined by the method given by Li et al. [23]

Nonequilibrium is accounted for in the VDF with the terms $\tau f_l^{eq}(a_l \xi_x + A_l)$ and $\tau f_r^{eq}(a_r \xi_x + A_r)$ in Equation (47). As long as $\tau f_{l,r}^{eq}(a_{l,r} \xi_x + A_{l,r}) \ll 1$, the approximation given here for the VDF is consistent with the first-order Chapman-Enskog expansion, and therefore recovers the NS equations.

If a NS cell has a neighbor Boltzmann cell, then the NS cell is given a velocity grid identical to the neighboring cell, and the VDF $f_0 = f_{l,r}^{eq}[1 - \tau(a_{l,r}\xi_n + A_{l,r})]$ is created on the cell interface where ξ_n is the normal velocity to the cell face (m/s). $f_{l,r}^{eq}$ is calculated using the macroparameters from the NS cell, and the coefficients for $a_{l,r}$ and $A_{l,r}$ are obtained using gradients of macroparameters from both cells.

The CFL (Courant–Friedrichs–Lewy) condition is used to determine the time step for both the Euler and NS solvers. Since all of the simulations presented in this work are unsteady, each cell uses the same time step (the minimum time step for the entire domain). The CFL condition is

$$\Delta t = \frac{\text{CFL} \times h}{\max(|U + 3\sqrt{T}|, |U - 3\sqrt{T}|)} \tag{53}$$

where Δt is the non-dimensional time step, h is the local non-dimensional cell size, U is the non-dimensional flow velocity defined as $U^2 = u^2 + v^2 + w^2$, T is the non-dimensional temperature, and $\max(|U + 3\sqrt{T}|, |U - 3\sqrt{T}|) = |\xi_{max}|$ for the

25

Boltzmann solver with ξ_{max} being the non-dimensional molecular velocity. The CFL is typically set to 0.5. The time required to run each simulation is reported in Chapter IV.

A well-known consequence of the BGK model is that the Prandtl number can only be unity [37]:

$$Pr = \frac{c_p \mu}{k} = 1 \tag{54}$$

where c_p is the specific heat at constant pressure (J/kg·K), and k is the coefficient of thermal conductivity (W/m·K). The Prandtl number is the ratio of the viscous diffusion rate to the thermal diffusion rate, and provides an indication of the relative importance of each. Thermal diffusion considers the transfer of energy through conduction, while viscous diffusion refers to the transfer of energy due to molecular mixing. When using the BGK model (including the kinetic-based NS solver), one can accurately model *either* viscosity μ *or* the coefficient of thermal conductivity k, but not both. Xu presents a Prandtl number fix based on altering the heat flux Q (W/m^2) (see Equation (16)) [39]. The energy flux (the last term in the vectors $\boldsymbol{F}$, $\boldsymbol{G}$, and $\boldsymbol{H}$) is modified by adding the correction term $(Pr^{-1} - 1)Q$ to it, where Q is calculated on the cell faces using polynomial interpolation of the VDF, and Pr is a variable Prandtl number. Results are reported for shockwave structure, showing that the regular NS solver (based on fluid continuum assumptions) and the kinetic-based NS solver show good agreement [24, 39].

Since UFS is a hybrid code, it has kinetic solvers in addition to the kinetic-based continuum solvers. The kinetic solver used in this work is the BGK model. However, since the BGK model does not calculate a collision integral, it does not inherently have the capability to account for internal molecular energies, and is only used for the Argon simulations. In order to retain the computational efficiency of the BGK model, UFS uses a three-temperature BGK (3T-BGK) model for flows involving internal energies (utilized for the N_2 simulations). Most of the details of this model

are not available for public release since UFS is regulated by ITAR (International Traffic in Arms Regulations). However, as a brief introduction, the 3T-BGK model assumes that there are three different temperatures T_{tr} (K) (translational), T_{rot} (K) (rotational), and T_{vib} (K) (vibrational).[9] The equilibrium temperature T^{eq} (K) can be obtained from a weighted average of the temperatures:

$$T^{eq} = \frac{3T_{tr} + K_r T_{rot} + K_v T_{vib}}{3 + K_r + K_v^{eq}} \tag{55}$$

where K_r and K_v are the rotational and vibrational degrees of freedom, respectively, and $K_v^{eq} = K_v(T^{eq})$.[10] The Maxwellian VDF f^{eq} is then calculated as

$$f^{eq} = f^{eq}(T_{tr})f^{eq}(T_{rot})f^{eq}(T_{vib}) \tag{56}$$

which assumes that the VDFs for each of the three temperatures are statistically independent of one another.

In order to successfully couple a continuum solver with a kinetic solver, a switching parameter is required. Such a parameter could indicate if the continuum assumption is appropriate for any given cell. Hence, the switching parameter is also sometimes referred to as the continuum breakdown parameter. As mentioned by Kolobov et al., it is important to use an appropriate switching parameter in order to avoid negative values in the VDF (which is non-physical) [21]. For example, Schrock and Carr both investigated entropy generation as a means of quantifying continuum

---

[9]Josyula et al. used a three-temperature BGK model as well, but the three temperatures were instead translational temperatures T_x, T_y, and T_z [19]. Also, Josyula et al. implemented a two-temperature BGK model for the translational and rotational temperatures, T_{tr} and T_{rot} [18].

[10]N_2 has two (not three) rotational degrees of freedom ($K_r = 2$). If the N_2 molecule is modeled as a dumbbell (or rigid rotor), then the energy of rotation about the axis which passes through the connector is very small compared to the energy of rotation through the other two principal axes. N_2 has three vibrational degrees of freedom ($K_v = 3$).

breakdown [7,34]. The switching parameter used in the first part of this work is

$$S_{NS} = Kn\sqrt{\left(\frac{\nabla p}{p}\right)^2 + \frac{1}{U^2}\left[\left(\frac{\partial u}{\partial x}\right)^2 + \left(\frac{\partial v}{\partial y}\right)^2 + \left(\frac{\partial w}{\partial z}\right)^2\right]} \tag{57}$$

where all values are non-dimensional, and $U^2 = u^2 + v^2 + w^2$, has been shown by Kolobov et al. to correctly couple the solvers near a shockwave at moderate Knudsen numbers [21]. A user-specified threshold value for S_{NS} is provided in an input file, and S_{NS} is calculated for each cell. If a cell's value for S_{NS} is larger than the threshold, then that cell is flagged as a Boltzmann cell. Otherwise, it is flagged as a continuum cell. Thus, by decreasing the S_{NS} threshold value, one decreases the number of continuum cells in the domain, while increasing the threshold value makes the Boltzmann region(s) smaller.

The threshold value used for the entropy-shock interaction study is based on the density gradient and local Knudsen number [21,32]:

$$S_\rho = Kn\frac{|\nabla\rho|}{\rho} \tag{58}$$

since the entropy spot has an accompanying density fluctuation profile.

III. Methodology

3.1 Shock Structure

In order to study shock structure using UFS, it was determined that a stationary two-dimensional shock should be used. It was thought that perhaps a shocktube domain should be used, since the Alsmeyer data was collected in a shocktube [3]. However, the increased computational cost of resolving the expansion wave and the contact surface, as well as the expanded domain that would be required made it undesirable. Therefore, the shock reference frame was chosen over the laboratory reference frame. Besides, the structure of the shock is more easily observed in the shock reference frame, which remains stationary. Since UFS is built on the Gerris software, which uses quadtree finite-volume discretization in two-dimensional physical space, the only way to have a one-dimensional simulation is to require that all of the cells have the same dimensions. If one is *only* interested in one-dimensional shock structure, then this grid is perhaps a good option. But, a goal of this research is to first study shock structure, and then to study how imperfections in the upstream flow (such as a spot of entropy) affect both the shock and the downstream flow characteristics. Such a study requires a two-dimensional physical domain.

Multiple grids (coarse, medium, and fine) were used to determine grid convergence in physical space. Figure 4 shows the coarse, medium, and fine grids for the Argon and Nitrogen simulations. The dimensions of the large cells for the medium grids are $\Delta_0 = \Delta x_0 = \Delta y_0 = \lambda_1$ (the upstream mean free path), and the small cells are of dimension $\Delta_2 = \Delta x_2 = \Delta y_2 = \lambda_1/4$, where Δ_0 is the dimension for base cells (m) (refinement Level 0) and Δ_2 is the dimension for cells of refinement Level 2 (m).[1] For the coarse grids, $\Delta_0 = 2\lambda_1$ and $\Delta_2 = \lambda_1/2$. For the fine grids, $\Delta_0 = \lambda_1/2$ and $\Delta_2 = \lambda_1/8$. The reference length L_{ref} (m), or the length by which all other lengths are normalized, is $L_{ref} = \Delta_0$ for each of the grids. The

---

[1]UFS is built on the Gerris software, which uses Cartesian quadtree (or octree for three dimensions) finite volume discretization. All cells are squares, and the base (or largest) cells are considered Level 0 ($\Delta_0/L_{ref} = 2^{-0} = 1$). More refined cells have higher levels of refinement, with $\Delta_n/L_{ref} = 2^{-n}$.

(a) Argon (Coarse)

(b) Argon (Medium)

(c) Argon (Fine)

(d) Nitrogen (Coarse)

(e) Nitrogen (Medium)

(f) Nitrogen (Fine)
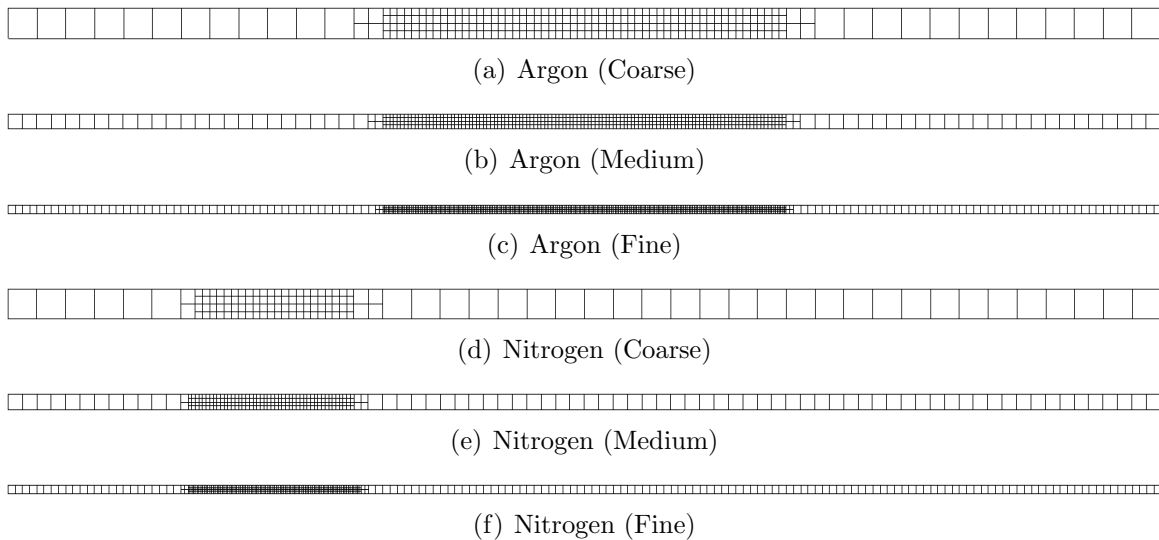
Figure 4: Coarse, medium, and fine grids in physical space.

medium grid for Argon is $80\lambda_1 \times \lambda_1$ with the standing shock located halfway between the upstream and downstream boundaries ($40\lambda_1$ away from both boundaries), where the flow is from left to right. The refined area is $14\lambda_1$ upstream and downstream of the shock, respectively. The medium grid for N_2 is $80\lambda_1 \times \lambda_1$. The shock is located $20\lambda_1$ from the upstream boundary, with refined regions $7.5\lambda_1$ upstream and $4.5\lambda_1$ downstream of the shock, respectively. In all cases, the medium grids were found to provide sufficient accuracy (the density profiles of the medium and fine grids were within 1% at every point for both the Argon and Nitrogen simulations), and were therefore used for the results presented in Chapter IV.

A value of $S_{NS} = 0.001$ was chosen for the Argon and Nitrogen simulations, with the subsequent domain decomposition shown in Figure 5 (cells in light blue are flagged as continuum cells, while cells in yellow are flagged as Boltzmann cells). The Boltzmann domain upstream of the shock increases with increasing Mach number due to the $1/U^2$ term in Equation (57), while the Boltzmann domain downstream of the shock decreases due to the predicted thinning of the shock by the BGK model. This result will be further discussed in Chapter IV. The domain decomposition for the Nitrogen cases are shown in Figure 6 for the same threshold value $S_{NS} = 0.001$ and color coding as in Figure 5. The same observations can also be made here, namely
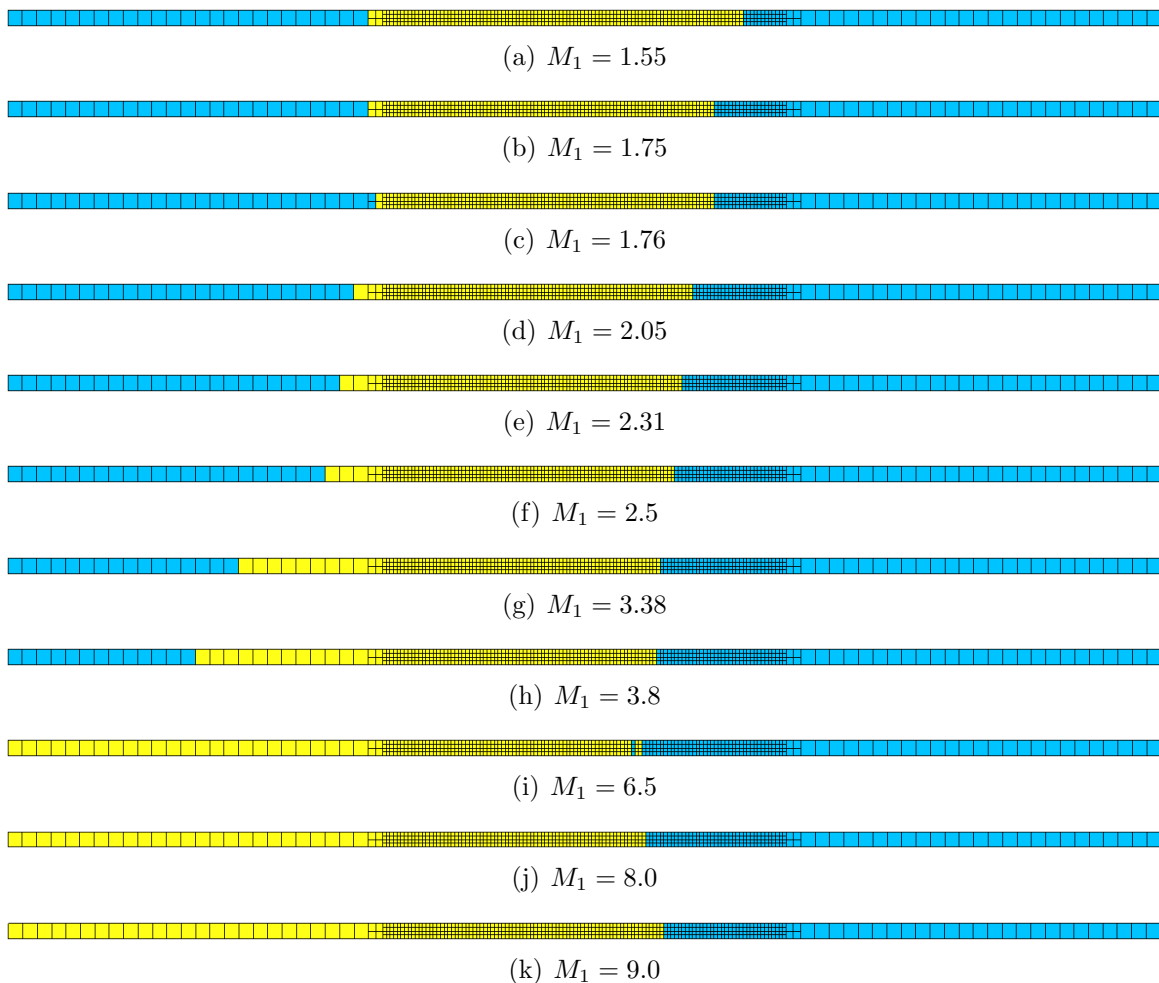
Figure 5: Visualizations of Boltzmann (yellow) and continuum (light blue) cells in Argon at steady-state with $S_{NS} = 0.001$. The shock is located in the middle of the refined grid region.

that the upstream Boltzmann domain increases with increasing Mach number, while the downstream Boltzmann domain decreases due to the predicted thinning of the shock.

A convergence study was performed on the switching parameter S_{NS} to determine if $S_{NS} = 0.001$ accurately reflects the full Boltzmann solution. All of the cases were simulated with only the Boltzmann solver turned on (either BGK or 3T-BGK), with no more than a 1% difference in density values between them and the results from the coupled solvers.
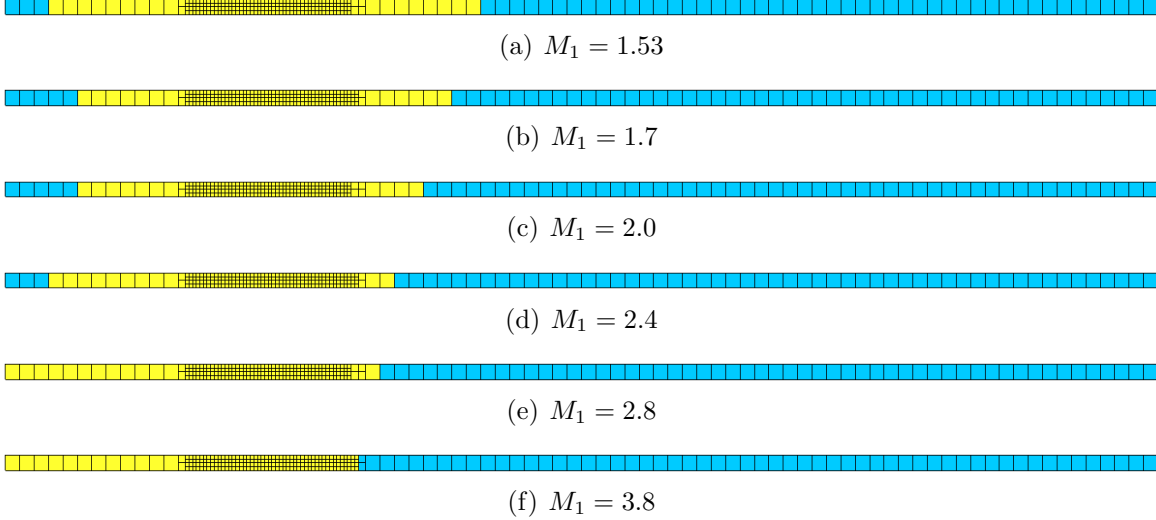
Figure 6: Visualizations of Boltzmann (yellow) and continuum (light blue) cells in N_2 at steady-state with $S_{NS} = 0.001$. The shock is located in the middle of the refined grid region.

Also, a grid independence study was performed in velocity space. For the Argon simulations on the medium velocity grid, the range in velocity space was $-8V_{ref}$ to $12V_{ref}$ with a node spacing of $0.2V_{ref}$ for $M_1 < 8$, and $-15V_{ref}$ to $15V_{ref}$ with a node spacing of $0.3V_{ref}$ for $M_1 \geq 8$ in both the u- and v-directions (100×100 nodes), where V_{ref} is the reference velocity (m/s), chosen here to be the upstream non-dimensional thermal velocity, defined as $\sqrt{2RT_1}$, where the upstream temperature T_1 is non-dimensionalized by the reference temperature T_{ref} (K). The fine and coarse grids had twice and half as many nodes as the medium grid, respectively. The density values differed by less than 1%. For the Nitrogen simulations on the medium velocity grid, the range in velocity space varied more with M_1 ($\pm 5V_{ref}$ with 20×20 nodes for $M_1 \leq 2$, $\pm 6V_{ref}$ with 24×24 nodes for $M_1 = 2.4$, $\pm 7V_{ref}$ with 28×28 nodes for $M_1 = 2.8$, and $\pm 9V_{ref}$ with 36×36 nodes for $M_1 = 3.8$), while the spacing was kept at $0.5V_{ref}$ in the u- and v-directions. The fine and coarse velocity grids had half and double the spacing in the medium grid, respectively. Density values for the medium grids all agreed with those for the fine grids within 1%, showing sufficient convergence.

For the Argon cases, Mach numbers $M_1 = 1.55$, 1.75, 1.76, 2.05, 2.31, 2.5, 3.38, 3.8, 6.5, 8.0, and 9.0 are investigated with an upstream temperature and density of 300 K and 6.63×10^{-6} kg/m^3, respectively, a Prandtl number of 2/3, a molecular mass of 39.948 amu, and a molecular diameter of 4.17×10^{-10} m [6].[2] The reference temperature, length, and time are $T_{ref} = 300$ K, $L_{ref} = 0.01721$ m, and $t_{ref} = 4.89 \times 10^{-5}$ s, respectively. The second-order coupled unsteady BGK and NS solvers are used with the minmod limiter. The switching parameter value is $S_{NS} = 0.001$. The NS solver is only turned on for the first 7000 iterations, at which point the NS and BGK solvers are coupled together until the shock is fully developed at $t = 0.0046$ seconds.

The computational domain is initialized with the Rankine-Hugoniot jump conditions for a shockwave [42]:

$$\rho_1 u_1 = \rho_2 u_2 \tag{59}$$

$$p_1 + \rho_1 u_1^2 = p_2 + \rho_2 u_2^2 \tag{60}$$

$$h_1 + \frac{u_1^2}{2} = h_2 + \frac{u_2^2}{2} \tag{61}$$

where $h = e + p/\rho$ is the specific enthalpy (J/kg), and e is the specific internal energy (J/kg). The computational domain is split into two regions: upstream and downstream of the shock. From the upstream Mach number M_1, density ρ_1, and temperature T_1, the rest of the flow parameters are determined. The left and right boundaries are set at their respective jump conditions for the duration of the simulation. Once the domain is initialized, however, the shock needs to develop, since it has a finite thickness (even if one is using an Euler solver). Therefore, the simulation is started with only the continuum solver turned on for a sufficient number of iterations. Once the shock is developed using the continuum solver, the Boltzmann solver is also

<hr>

[2]The Argon and Nitrogen upstream Mach numbers were chosen to match those reported by Alsmeyer [3].

33

turned on (coupled solvers) and the domain is allowed to arrive at a steady-state solution.

The jump conditions are derived only from the laws of conservation of mass, momentum, and energy, respectively, and therefore make no assumptions about the type of gas being considered (e.g. ideal gas). However, the Rankine-Hugoniot jump conditions *do* assume that the shockwave is a mathematical discontinuity in space (has zero thickness), and therefore are not entirely exact. In other words, viscosity and heat conduction are not accounted for in Equation 61, which assumes that the flow is adiabatic (or that entropy is constant along streamlines). In reality, entropy increases through the shock due to nonequilibrium, with the result that the entropy downstream is larger than the entropy upstream of the shock. However, it is assumed that these jump conditions provide adequate boundary conditions for the flow.

For the Nitrogen cases, Mach numbers $M_1 = 1.53$, 1.7, 2.0, 2.4, 2.8, and 3.8 are investigated with an upstream temperature and density of 300 K and 1.0×10^{-3} kg/m^3, respectively, a Prandtl number of 0.69, a molecular mass of 28.0 amu, and a molecular diameter of 4.17×10^{-10} m [6]. Initially, upstream Mach numbers up to 10.0 were included in this study, but due to the computational times required (about 2 weeks for one simulation) as well as the memory requirements, it was determined that only Mach numbers up to 3.8 would be considered. The second-order coupled unsteady 3T-BGK and Euler solvers are used with the minmod limiter. The NS solver is not currently capable of handling internal degrees of freedom, so the Euler solver is used instead for the continuum regions. The vibrational characteristic temperature Θ_v is 3,371 K.[3] The rotational collision number Z_{rot} is 5, and the vibrational collision number Z_{vib} is 7.9×10^7, calculated from Bird's restatement of Millikan and White's

---

[3]Θ_v is the temperature at which vibrational energy contributions become significant, Z_{rot} is the number of collisions required to fully transfer rotational energy, and Z_{vib} is the number of molecular collisions required to equilibrate the vibrational energy.

curve fit to experimental data [6, 27]:[4]

$$Z_{vib} = \frac{C_1}{T^\omega} e^{C_2 T^{-1/3}} \tag{62}$$

where the constants C_1 and C_2 for N_2 are 9.1 and 220.0, respectively, and the viscosity index ω is 0.74. The switching parameter value remains $S_{NS} = 0.001$. The Euler solver is used again for the first 7000 iterations, at which point the Euler and 3T-BGK solvers are coupled until the shock is fully developed at $t = 0.076$ seconds.

The Prandtl number is here calculated using Eucken's relation [38]:

$$Pr \approx \frac{4\gamma}{7.08\gamma - 1.80} \tag{63}$$

which gives $Pr = 0.69$ for $\gamma = 1.40$ (diatomic), and $Pr = 2/3$ for $\gamma = 1.67$ (monatomic), where γ is the ratio of specific heats $\gamma \equiv c_p/c_\nu$.[5] These approximate values are adequate for the current study, even though it is recognized that γ is not constant through the temperature ranges considered.[6]

Comparison of UFS simulations is made with Alsmeyer experimental data and with Bird's educational DSMC code, DSMC1S, which is tailored specifically for one-dimensional shock structure calculations [3]. Alsmeyer reported density data in Argon and Nitrogen from a shocktube using the absorption of an electron beam, with an apparatus similar to the one developed by Schmidt [33]. The electron beam apparatus was located near the far wall of the shocktube, and is relatively unobtrusive. Density, temperature (translational and rotational), the axial heat flux coefficient, and the partially-integrated VDF profiles, shock thickness, and the density asymmetry factor are calculated and presented for all the simulations in this shock structure analysis.

---

[4]According to Jain, Z_{rot} for N_2 over the temperatures considered is between 4 and 5 [17].

[5]Eucken arrived at his empirical correlation by altering the result from kinetic theory, $Pr \approx 4\gamma/(15\gamma - 15)$.

[6]According to White, $0.66 \leq Pr \leq 0.68$ for Argon (a difference of 3%), and $0.69 \leq Pr \leq 0.73$ for N_2 (a difference of 5%) in the temperature ranges considered [38].

In order to determine how well two density profiles match, the inverse shock thickness δ, based on the maximum density gradient, has been defined as [37]

$$\delta = \frac{\lambda_1}{\bar{x}_\rho} = \frac{\lambda_1 \left(\dfrac{d\rho}{dx}\right)_{max}}{\rho_2 - \rho_1} \tag{64}$$

where the maximum density gradient is found with a second-order scheme:

$$\left(\frac{d\rho}{dx}\right)_{max} = \frac{\rho_{i+1} - \rho_{i-1}}{2\Delta x} + O(\Delta x^2) \tag{65}$$

Bird gives the upstream equilibrium mean free path λ_1 as [6]

$$\lambda_1 = \frac{2(5 - 2\omega)(7 - 2\omega)}{15} \left(\frac{m}{2\pi kT}\right)^{1/2} \frac{\mu}{\rho} \tag{66}$$

where ω is the viscosity index, μ is the viscosity, ρ is the density, k is the Boltzmann constant, and m is the molecular mass. To non-dimensionalize the experimental data, Alsmeyer calculated λ_1 based on the HS kinetic model ($\omega = 1/2$):

$$\lambda_1 = \frac{16}{5} \left(\frac{m}{2\pi kT}\right)^{1/2} \frac{\mu}{\rho} \tag{67}$$

The UFS data is processed using this formulation of λ_1. Bird's code DSMC1S also uses the HS model for the molecules ($\omega = 0.81$ for Argon, $\omega = 0.74$ for Nitrogen), and actually outputs λ_1 (0.01304 m for Argon, 0.01324 m for Nitrogen). By noticing that

$$\frac{\lambda_{1,\text{alsmeyer}}}{\lambda_{1,\text{bird}}} = \frac{24}{(5 - 2\omega)(7 - 2\omega)} \tag{68}$$

and

$$\lambda_{1,\text{alsmeyer}} = \lambda_{1,\text{bird}} \left(\frac{\lambda_{1,\text{alsmeyer}}}{\lambda_{1,\text{bird}}}\right) \tag{69}$$

λ_1 for the UFS simulations is calculated to be 0.01721 m for Argon and 0.01635 m for Nitrogen. In order to compare DSMC results with those from UFS and the Alsmeyer data, it is necessary to use the same value of λ_1. Therefore, DSMC results are presented with $\lambda_1 = \lambda_{1,\text{alsmeyer}}$ instead of $\lambda_{1,\text{bird}}$.

From a density profile, one can construct $\bar{x}_\rho$ by extending the tangent to the curve at the maximum gradient location (ρ_n=0.5) to the horizontal lines $\rho_n = 1$ and $\rho_n = 0$, where the normalized density ρ_n is

$$\rho_n(x) \equiv \frac{\rho(x) - \rho_1}{\rho_2 - \rho_1} \tag{70}$$

The intersections of these lines are taken as the boundaries of the shock, and so the distance between them on the x-axis is the shock thickness $(1/\delta)$, shown in Figure 7. This inverse shock thickness does not take into account the skewness of the density
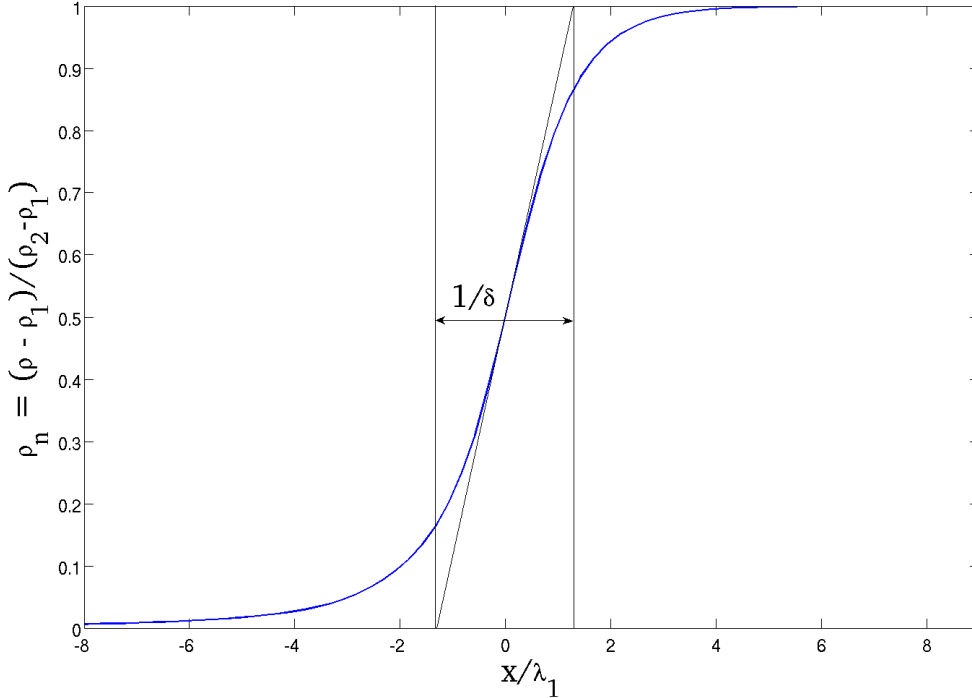
Figure 7: Construction of shock thickness $1/\delta$.

profile, or any other behavior upstream or downstream of the shock midpoint, which limits its usefulness.

Another value which can be computed is the density asymmetry factor Q:

$$Q \equiv \frac{\int_{-\infty}^{0} \rho_n(x)dx}{\int_{0}^{\infty} [1 - \rho_n(x)]dx} \tag{71}$$

which is calculated using a numerical trapezoidal method. Q takes into account the skewness of the density profile by dividing the area under the curve up to the shock midpoint by the area between the curve and the line $\rho_n = 1$ beginning at the shock midpoint. Figure 8 gives a visual representation of how Q is calculated (the area on the left divided by the area on the right). A value of unity signifies that the density profile is perfectly symmetric, while a value greater or less than unity indicates a profile skewed to the left or right, respectively.
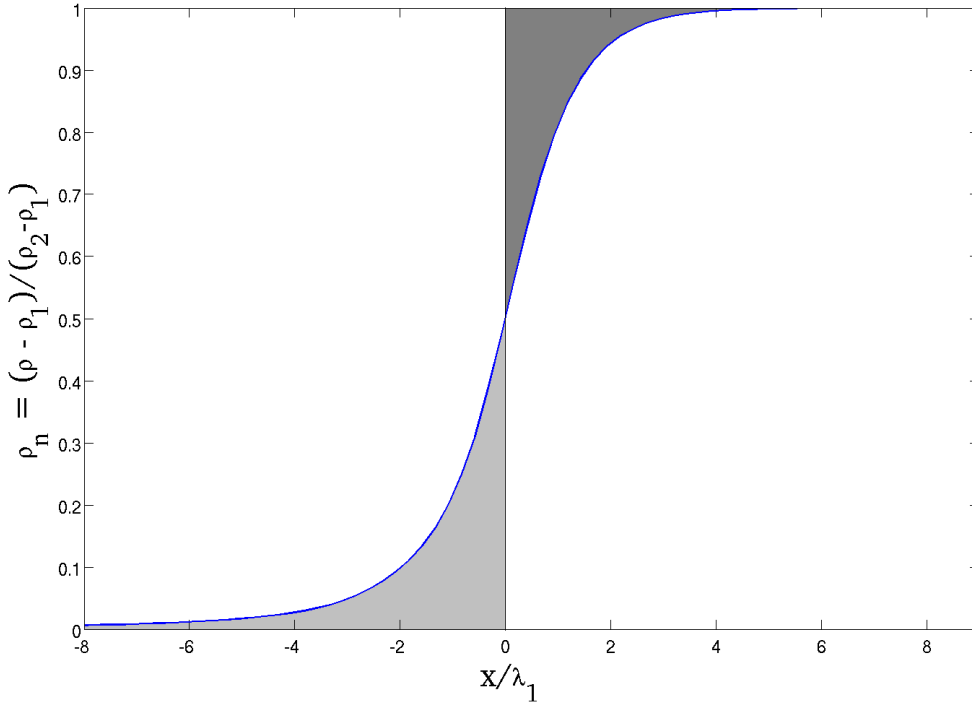
Figure 8: Construction of density asymmetry factor Q.

The overall flow temperature is not an output of UFS, so it is calculated from the non-dimensional pressure and density:

$$T^* = \frac{p^*}{\rho^*} \tag{72}$$

since $p^* = p/p_{ref}$, $\rho^* = \rho/\rho_{ref}$, $T^* = T/T_{ref}$, $p = \rho R T$, and $p_{ref} = \rho_{ref} R T_{ref}$. The normalized temperature profile T_n is then calculated from

$$T_n \equiv \frac{T - T_1}{T_2 - T_1} \tag{73}$$

where the non-dimensional superscript $*$ is dropped, and T_1 and T_2 are the upstream and downstream equilibrium temperatures, respectively. The rotational temperature T_{rot} is an output of UFS, so the normalized rotational temperature is calculated in the same way as the normalized overall temperature in Equation 73. UFS also outputs the vibrational temperature T_{vib}, but DSMC1S does not. Therefore, T_{vib} is not presented in this study.

The heat flux q_x, which is the flow of energy per unit area per unit time (W/m^2), is represented using the heat flux coefficient C_{q_x}:

$$C_{q_x} \equiv \frac{q_x}{\frac{1}{2}\rho_1 u_1{}^3} \tag{74}$$

The VDFs of this study are two-dimensional, but the VDFs from UFS are in terms of the u- and v-directions, while the VDFs from DSMC are in terms of the u- and radial-directions.[7] Therefore, the VDFs from UFS and DSMC cannot be compared directly. Instead, the data is presented in terms of a partially-integrated VDF f_x [6]:

$$f_x \equiv \int f \, dv \, dw \tag{75}$$

---

[7]DSMC1S assumes that the non-axial velocity is axially symmetric.

A few issues concerning the VDF were encountered with UFS. First, the VDF output from UFS is not normalized. To overcome this, the area under the curve is calculated, and then each point is divided by that total area. Second, since UFS is a relatively new code, when multiple processors are used in parallel, the only cells that output the VDF are those that are computed using the first processor. This drawback limits the results presented in Chapter IV because they were obtained on multiple processors. Finally, cells flagged as continuum cells do not calculate the VDF. So, when one is using UFS to couple continuum and Boltzmann solvers, some cells of interest may not output a VDF.

3.2 Entropy-Shock Interaction

Two models for the entropy spot were considered: a constant spot, and a Gaussian spot. The constant spot assumes a discontinuity at the spot boundary with constant entropy within the spot. Even though a constant spot may be easier to apply numerically, a more realistic model can be implemented. The Gaussian spot provides a greater degree of accuracy by assuming a Gaussian profile of the form [16]

$$\frac{T_1'}{T_1} = \epsilon\, e^{-r^2/2} \tag{76}$$

shown in Figure 9, where T' is the temperature perturbation within the entropy spot (K), ϵ is the perturbation amplitude (chosen to be 0.25), and r is the radius from the center of the entropy spot (m), defined as $r^2 = (x - x_c)^2 + (y - y_c)^2$ where x_c and y_c are the x- and y- coordinates of the center of the entropy spot, respectively (m). The local density is then calculated as[8]

$$\rho_1 + \rho_1' = \frac{p_1}{T_1 + T_1'} \tag{77}$$

---

[8]Pressure is constant in an entropy spot, while density and temperature fluctuate.

40

(a) Temperature   (b) Density
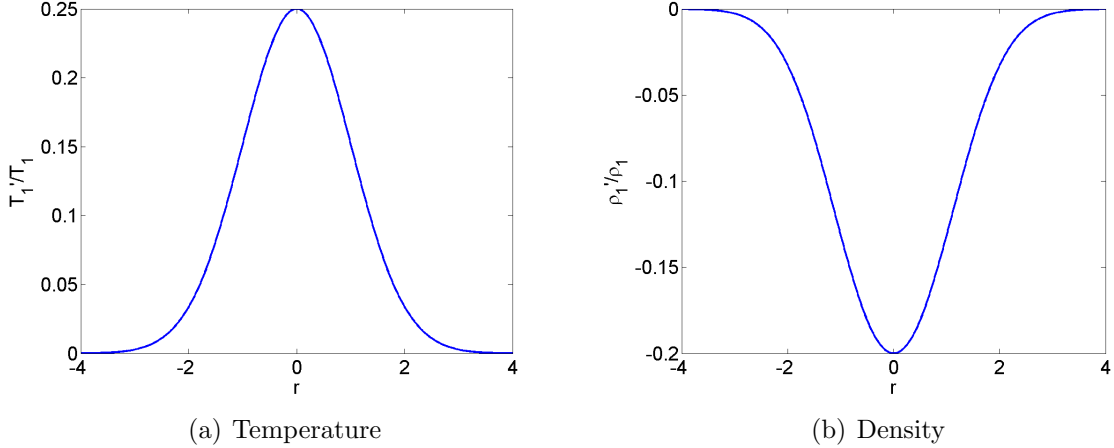
Figure 9: Entropy spot temperature and density profiles.

also shown in Figure 9. Note that even though the maximum temperature fluctuation is 25%, the minimum density fluctuation is only -20%.

The grid set-up is one box with dimensions $20a \times 20a$, where a is the radius of the entropy spot (m) (chosen to be $25\lambda_1$), shown in Figure 10. The vertical shock is located in the middle of the domain with the same upstream and downstream boundary conditions as in the shock structure study. The top boundary is a freestream boundary, while the bottom boundary is a symmetry boundary, effectively creating a domain that is $20a \times 40a$. The upstream Mach number is $M_1 = 2.0$ with the flow propagating from the left to the right. The center of the entropy spot is initially located five radii upstream of the shock on the symmetry centerline.

The flowfield is initialized in Argon with upstream and downstream values based on the Rankine-Hugoniot shock jump conditions, and then the shock is allowed to develop with just the NS solver, after which the shock is allowed to develop with the coupled BGK & NS solvers ($S_\rho = 0.01$) until it achieves a steady state.[9] Once the flowfield is thus computed (taken as $t = 0$), the entropy spot is inserted upstream of the shock and allowed to freely convect through the shock using the

---

[9] $Pr = 2/3$, molecular mass is 39.948 amu, molecular diameter is 4.17×10^{-10} m, $T_1 = 300$ K , $\rho_1 = 6.63 \times 10^{-6}$ kg/m^3 , $\lambda_1 = 0.01721$ m .
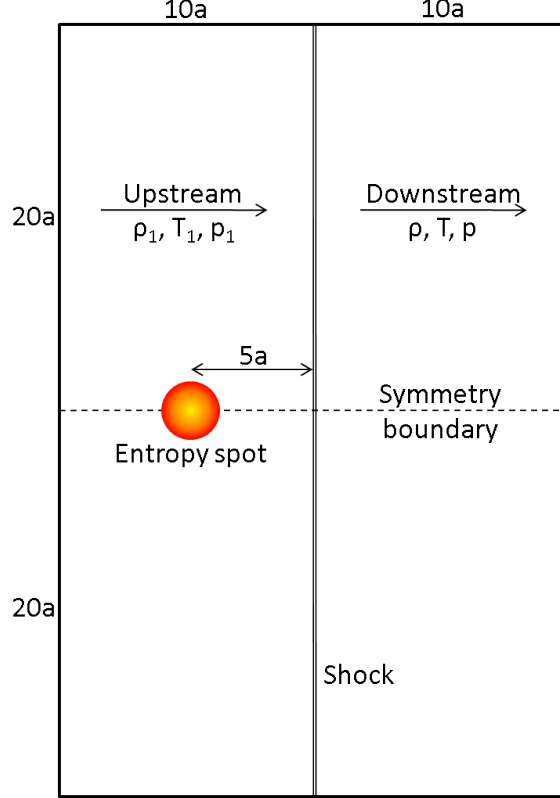
Figure 10: Grid set-up for entropy-shock simulation at $t = 0$ (adapted from [16]).

coupled BGK & NS solvers. Figure 11 shows the computational domain (colored by density) for $Kn = 0.1$ immediately after the entropy spot is introduced.

Three Knudsen numbers are investigated in order to study the effects of rarefaction on entropy-shock interactions. The Knudsen numbers were chosen to be within the continuum ($Kn = 0.01$), near-continuum ($Kn = 0.1$), and rarefied regimes ($Kn = 1.0$).

Grid studies in physical space were conducted on coarse, medium, and fine grids. The medium grid is refined up to Level 10 ($\Delta_0 = 500\lambda_1$, $\Delta_{10} \cong \lambda_1/2$) based on the spatial gradient of $(\ln \rho + \ln p)$. For the x-direction, if any cell has a gradient of the form

$$\frac{\partial}{\partial x}(\ln \rho + \ln p) = \frac{1}{\rho}\frac{\partial \rho}{\partial x} + \frac{1}{p}\frac{\partial p}{\partial x} \qquad (78)$$

42
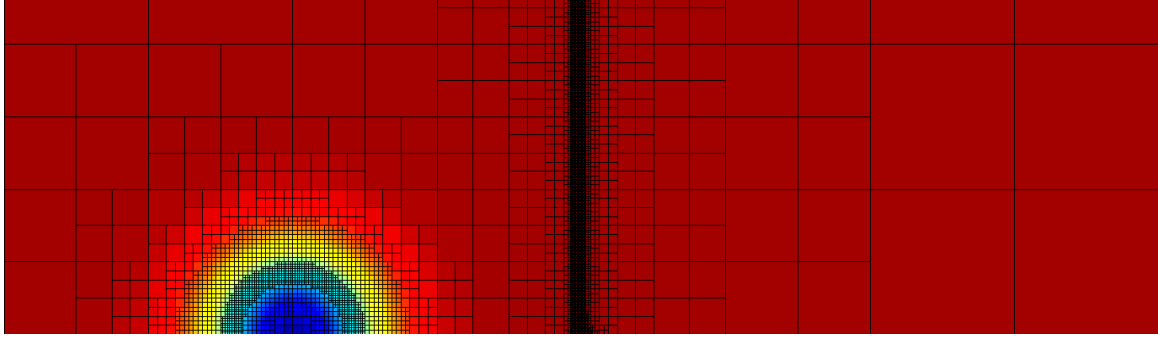
(a) Grid ($\rho_{min} = 0.80$, $\rho_{max} = 1.00$)
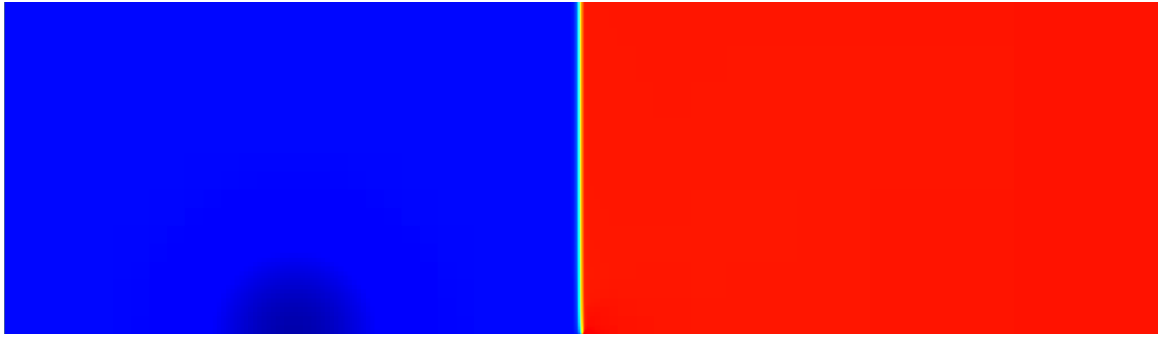
(b) No grid ($\rho_{min} = 0.80$, $\rho_{max} = 2.51$)

Figure 11: Initialization of the computational domain, colored by density ($Kn = 0.1$, medium physical and velocity grids). Only a portion of the domain is shown.

larger than 0.01 (or of 1%), then it is refined either until the gradient is less than 0.01 or it is refined to Level 10. The coarse grid is refined up to Level 9 ($\Delta_9 \cong \lambda_1$), and the fine grid is refined to Level 11 ($\Delta_{11} \cong \lambda_1/4$), with the same criterion on the gradient. The rarefied simulations ($Kn = 1.0$) had to be computed using only the coarse grid. It is possible that the medium and fine grids were unsuitable for the high Knudsen number due to the low number of molecules in each cell.[10] For $Kn = 0.01$, the density profiles agree within 3% between the fine and medium grids. For $Kn = 0.1$, the density profiles agree within 1% between the coarse and medium physical grids. No grid study was performed for $Kn = 1.0$ since the coarse grid was the finest grid that could be used.

---

[10]Molecular number density (number of molecules per unit volume) decreases with increasing Kn.

Velocity-space grid studies were also performed on coarse, medium, and fine grids. All of the grids have ranges of $-4V_{ref}$ to $6V_{ref}$ in the u-direction, and $-5V_{ref}$ to $5V_{ref}$ in the v-direction. The coarse grid has 10×10 nodes, the medium grid has 20×20 nodes, and the fine grid has 40×40 nodes. The node spacing is then V_{ref}, $0.5V_{ref}$, and $0.25V_{ref}$ for the coarse, medium, and fine grids, respectively. For $Kn = 0.01$ and 0.1, the density profiles agree within 0.1% between the fine and medium grids. No velocity grid study was performed for $Kn = 1.0$ due to non-physical results obtained on the coarse and fine grids. It is unclear why those simulations were unstable.

During simulations, it was found that numerical errors were created at the interfaces of the upper and lower boundaries and the shock. The upper boundary is far enough away from the entropy spot as to not be a concern. However, the numerical errors at the interface of the shock and the symmetry boundary (shown in Figure 12) make it difficult to analyze the data right at the symmetry plane.
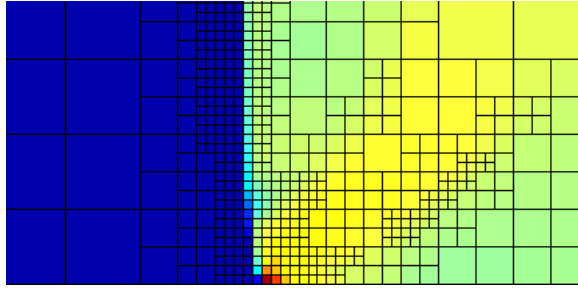
Figure 12: Numerical error introduced at the interface of the symmetry boundary and the shock in density.

Gradient profiles are presented for density, pressure, and temperature. A second-order scheme is used to compute the gradients as before:

$$\frac{\partial b}{\partial x} = \frac{b_{i+1} - b_{i-1}}{2\Delta x} + O(\Delta x^2) \tag{79}$$

where b represents density, pressure, or temperature.

No VDFs are presented since the only cells that output the VDF are Boltzmann cells, which are mainly in the shock structure.

IV. Results

4.1 Argon Shock Structure

Nanbu and Watanabe performed a study on the one-dimensional shock structure of a monatomic gas in 1984 using a new method to directly simulate the Boltzmann equation [29]. Ohwada also performed a numerical study of the Boltzmann equation for a monatomic gas (HS molecules) and even reported VDFs [30]. However, all of their results agreed well with those from Bird's method, so Bird's code DSMC1S is used here for direct comparison with the current results for both monatomic and diatomic molecules.

Normalized density profiles in Argon for various upstream Mach numbers have been presented by Alsmeyer, and are compared here with the results from UFS (coupled BGK & NS solvers) in Figures 13 and 14 [3]. Also presented are results from UFS using the NS solver in the entire domain, as well as DSMC results from Bird's code DSMC1S [6]. BGK agrees closely with experiment and DSMC up to about $M_1 = 3.38$, after which BGK deviates significantly by predicting a thinner shock.

The inverse shock thickness is plotted in Figure 15; larger values indicate a thinner shock, and vice versa. DSMC overpredicts shock thickness, although it is the most accurate method presented. The BGK model underpredicts shock thickness, deviating from experiment at about $M_1 = 2.5$, which agrees with the results presented by Schmidt, thus showing that the BGK model in UFS performs well [33]. The NS solver predicts the thinnest shocks, as expected, since NS only allows for small deviations from equilibrium.

The density asymmetry factor is plotted in Figure 16 with experimental values from Alsmeyer and Schmidt [3, 33]. The experimental results indicate that density profiles skew more to the left with increasing M_1. DSMC follows experiment fairly well, while the coupled UFS solver (BGK & NS) profiles are skewed much more to the left. The NS solver shows a relatively constant value for Q with the profiles being skewed to the left for all upstream Mach numbers.
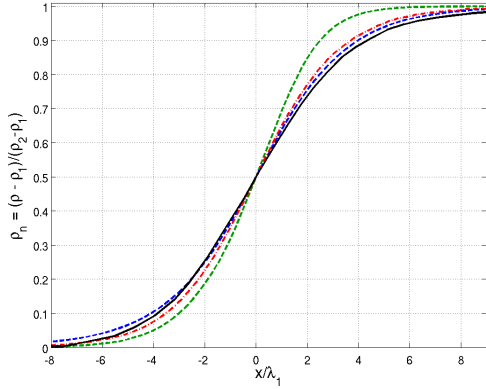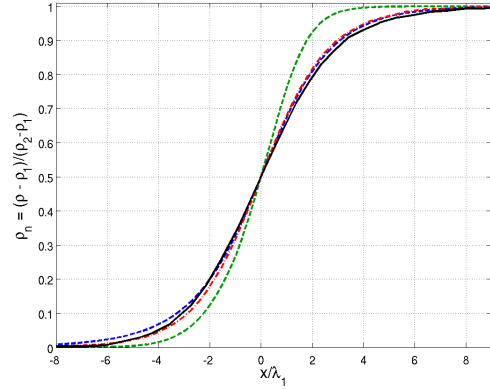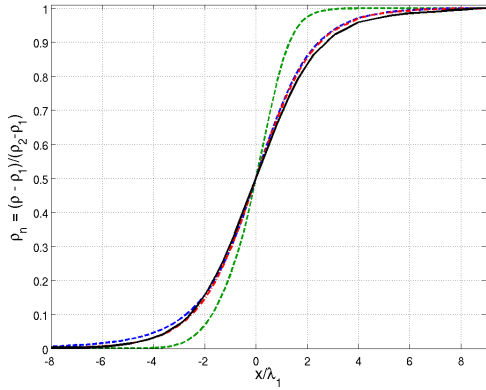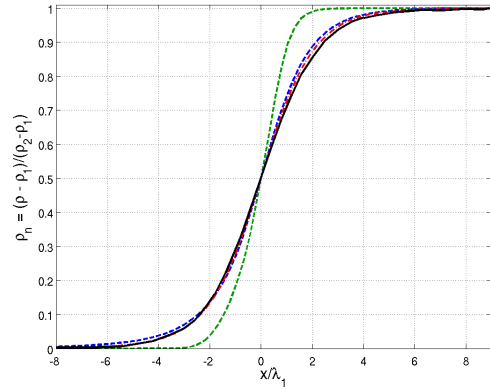
Figure 13: Density profiles in Argon. BGK & NS (blue); NS (green); DSMC (red); Alsmeyer (black).

The translational temperature T_{tr} profiles for Argon are shown in Figures 17 and 18 for the UFS coupled solver (BGK & NS), the UFS NS solver, and DSMC. Since Argon is monatomic, it has no internal energy modes (besides electronic, which is neglected in this study), and therefore the only molecular energy that can be transferred is kinetic (or translational), which means that these profiles also represent the overall temperatures in the flow. The temperature profiles have midpoint values upstream of the midpoint of the shock based on density. The NS profiles show larger gradients with increasing M_1 and provide limiting cases for comparison. Up to $M_1 = 3.8$,

(a) $M_1 = 3.38$

(b) $M_1 = 3.8$

(c) $M_1 = 6.5$

(d) $M_1 = 9.0$
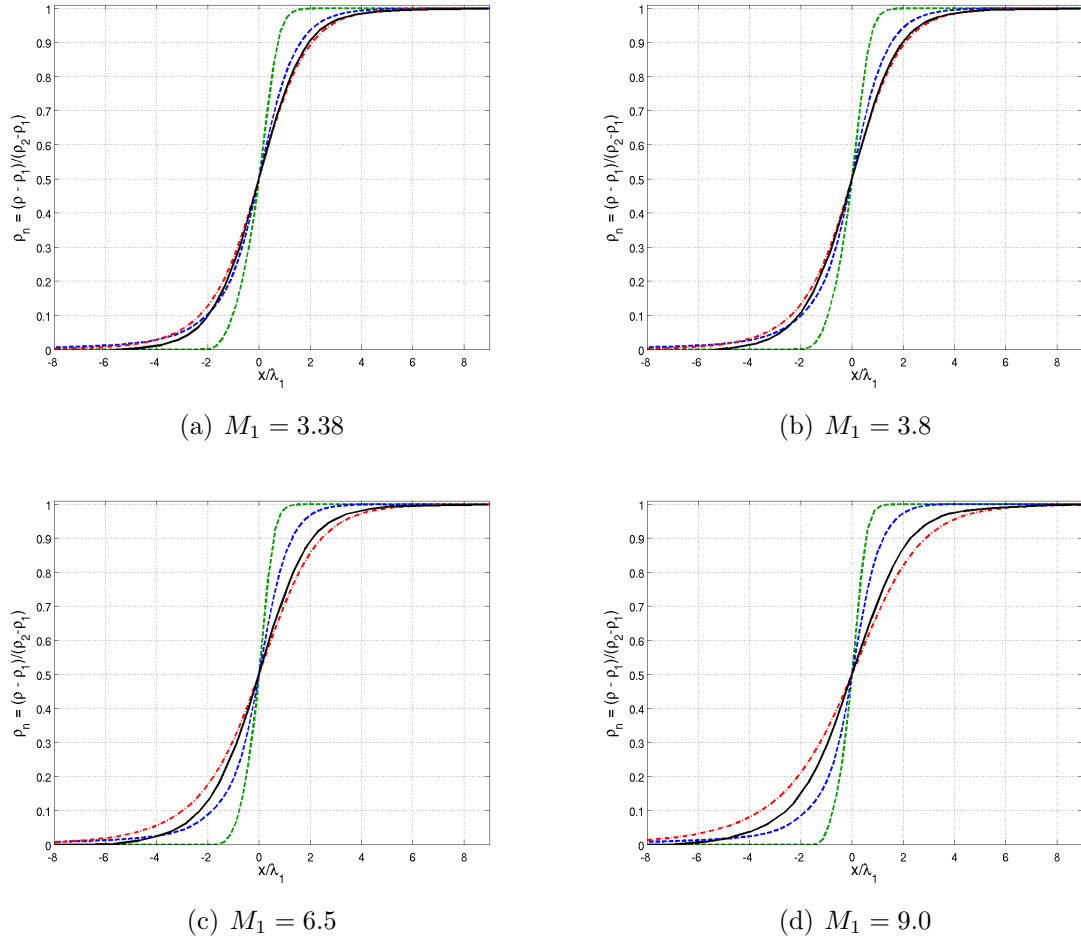
Figure 14: Density profiles in Argon. BGK & NS (blue); NS (green); DSMC (red); Alsmeyer (black).

DSMC and BGK & NS show good agreement, after which DSMC predicts a higher relaxation time.

The heat flux coefficient C_{q_x} is shown in Figures 19 and 20. The minima of the coupled UFS solver (BGK & NS) and the DSMC code are within 2% for all values of M_1, with the profiles matching well up to $M_1 = 3.8$. At higher upstream Mach numbers, DSMC shows higher relaxation times, an earlier onset of nonequilibrium, and minima which occur upstream of the BGK & NS minima.

The partially-integrated VDFs (f_x) are given in Figures 21 and 22 for the DSMC and BGK & NS solvers. Up to $M_1 = 2.5$, the profiles show very good agreement.
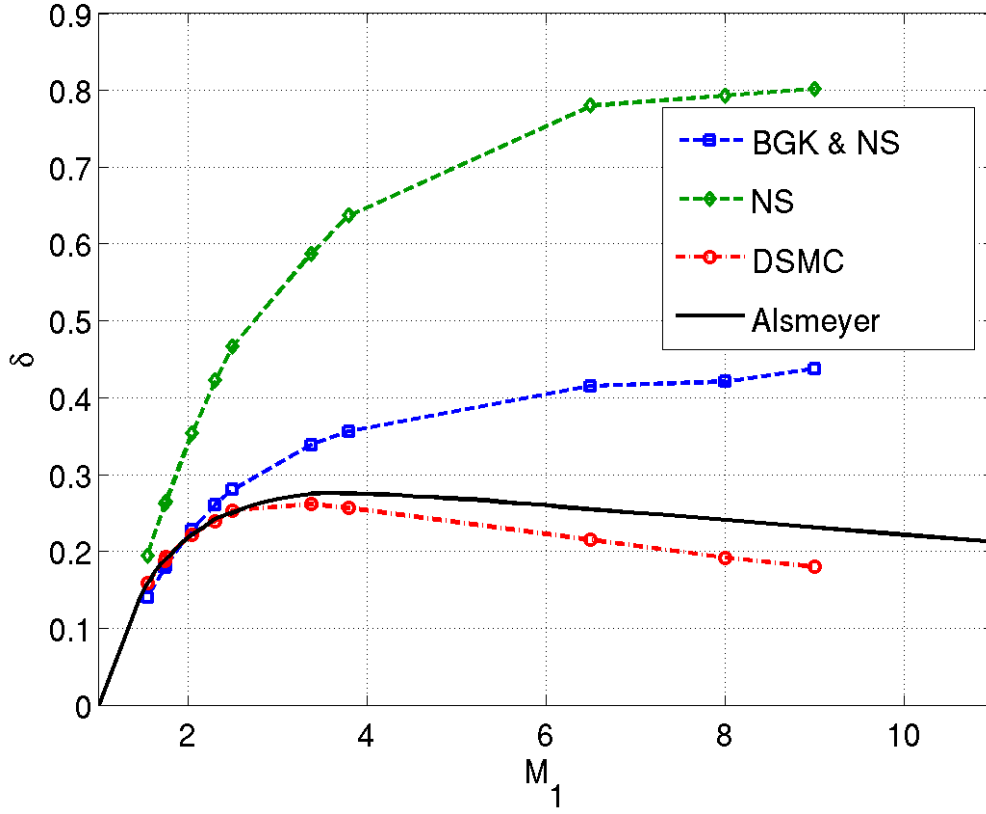
Figure 15: Inverse shock thickness δ for Argon.

At $M_1 = 3.38$ and 3.8, the profiles begin to show some deviation from one another with the BGK & NS profiles being skewed slightly more to the right than the DSMC profiles.

Even greater deviation is exhibited for $M_1 = 6.5$, 8.0, and 9.0. This can be explained by a phenomenon encountered during simulation, namely that the shock in UFS began to move upstream.[1] The other results (i.e. density, temperature, and heat flux) are unaffected by a moving shock since they all reference the density midpoint of the shock. However, the VDFs are output from UFS at specific locations in the domain, so the errors seen at $M_1 = 6.5$, 8.0, and 9.0 are apparent since the midpoint of the shock is not located at the center of the cell (but rather between two cells).

---

[1] A moving shock was not observed for the other Mach numbers.
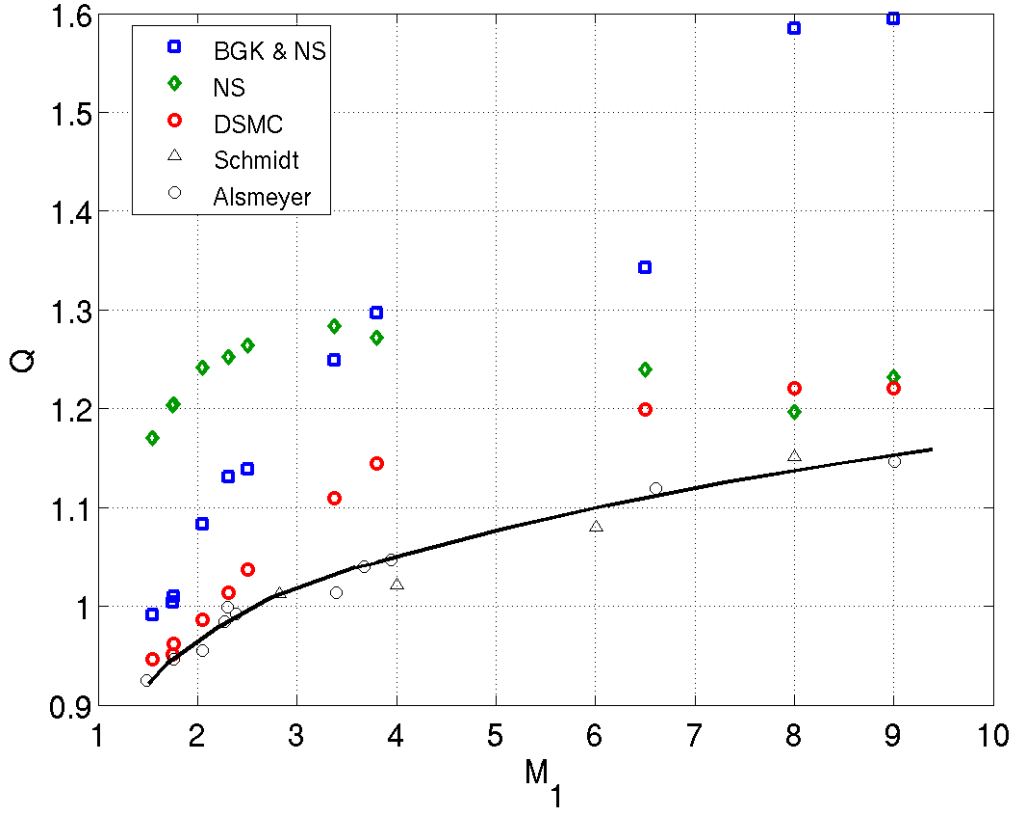
Figure 16: Density asymmetry Q in Argon. The solid curve is from Alsmeyer [3].

From the previous results, it is clear that for these Mach numbers, DSMC predicts greater nonequilibrium farther upstream than BGK & NS, indicating that the DSMC VDF evolves more slowly than the BGK & NS VDF as the gas convects through the shock. Therefore, the BGK & NS VDF at $x/\lambda_1 = -1.5$ has a higher maximum than the DSMC VDF, and a lower maximum than the DSMC VDF at $x/\lambda_1 = 0.0$.

The total number of hours required to run each simulation (including the grid independence studies) is shown in Figure 23 versus the upstream Mach number M_1. At $M_1 = 1.55$ the time step is 0.229 μs, while at $M_1 = 9.0$ the time step is 0.161 μs.

For UFS, the run times are relatively constant up to $M_1 = 6.5$, at which point they increase exponentially, as shown on the logarithmic scale. The DSMC simulations took from 1 to 2 hours to complete, while the UFS simulations required up to 122
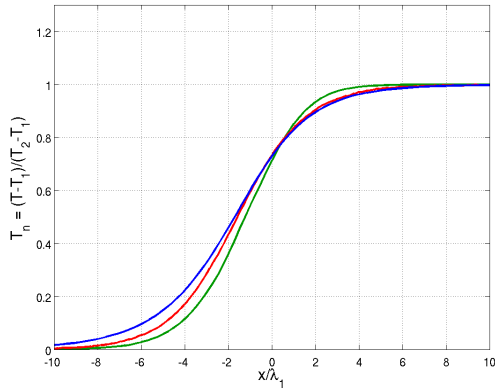
(a) $M_1 = 1.55$
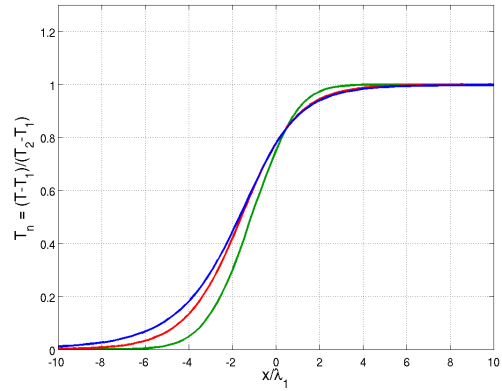
(b) $M_1 = 1.75$
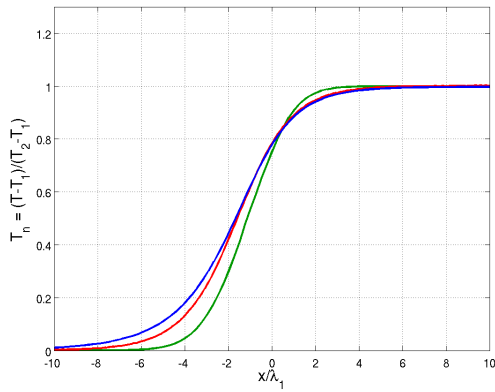
(c) $M_1 = 1.76$
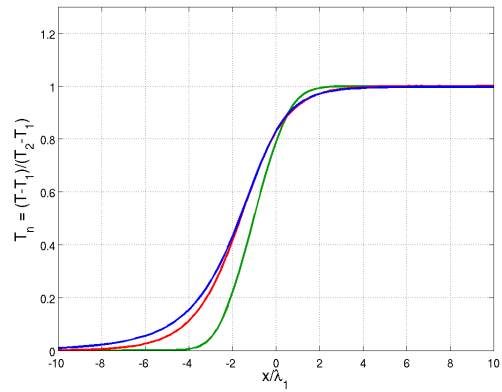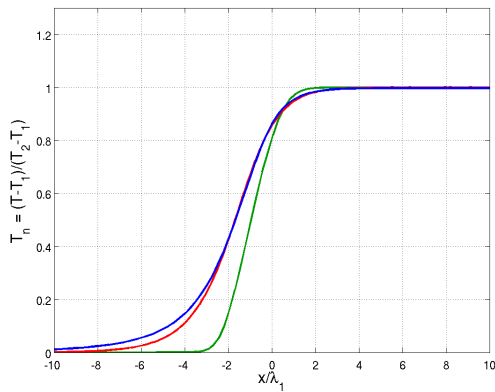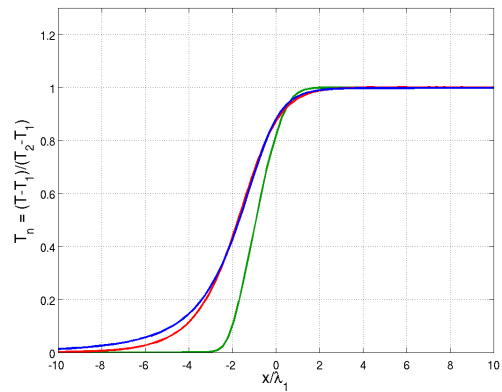
(d) $M_1 = 2.05$

(e) $M_1 = 2.31$

(f) $M_1 = 2.5$

Figure 17: Translational temperature profiles in Argon. BGK & NS (blue); NS (green); DSMC (red).
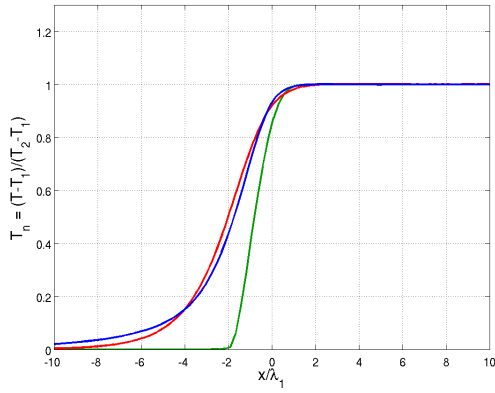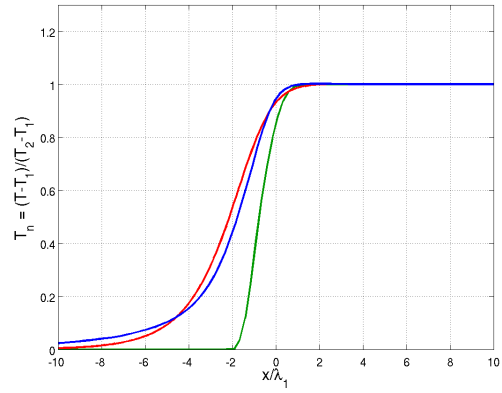
(a) $M_1 = 3.38$

(b) $M_1 = 3.8$
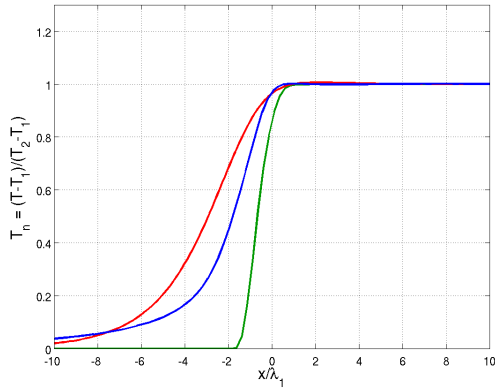
(c) $M_1 = 6.5$
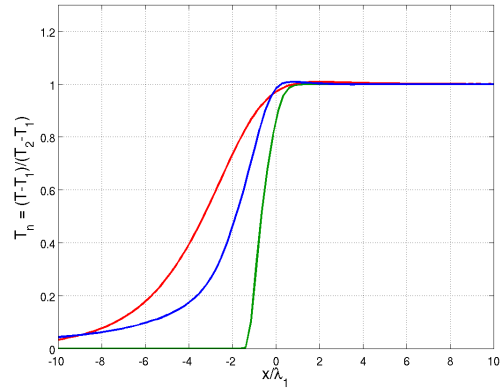
(d) $M_1 = 8.0$
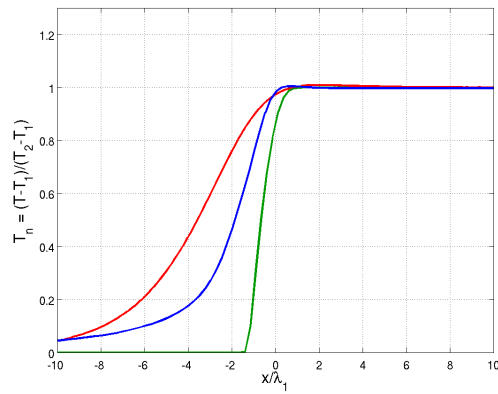
(e) $M_1 = 9.0$

Figure 18: Translational temperature profiles in Argon. BGK & NS (blue); NS (green); DSMC (red).
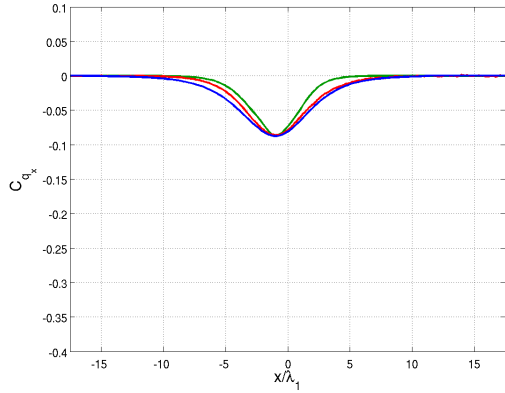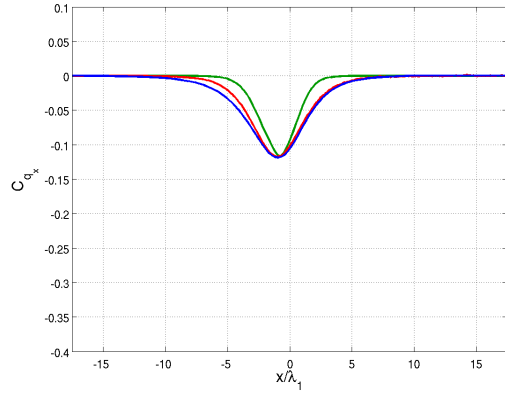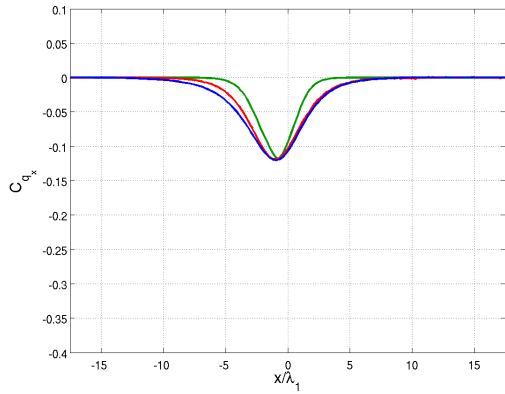
(a) $M_1 = 1.55$
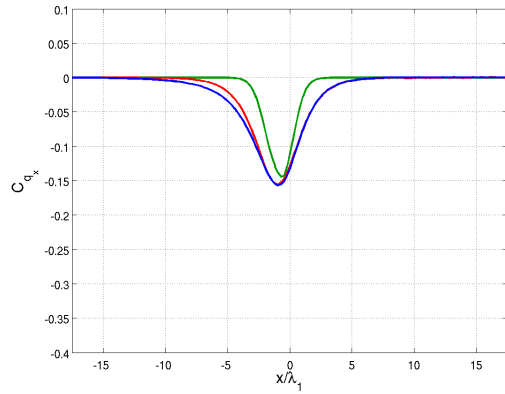
(b) $M_1 = 1.75$
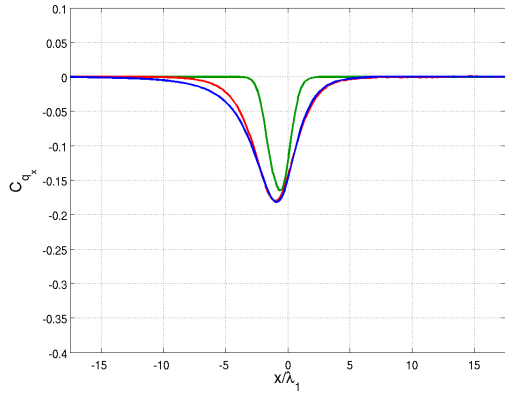
(c) $M_1 = 1.76$
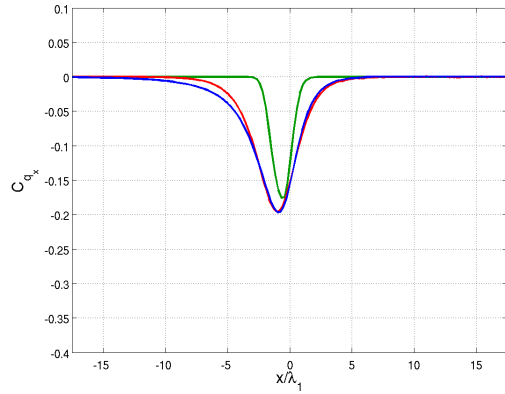
(d) $M_1 = 2.05$

(e) $M_1 = 2.31$

(f) $M_1 = 2.5$

Figure 19: Heat flux coefficient profiles for q_x in Argon. BGK & NS (blue); NS (green); DSMC (red).
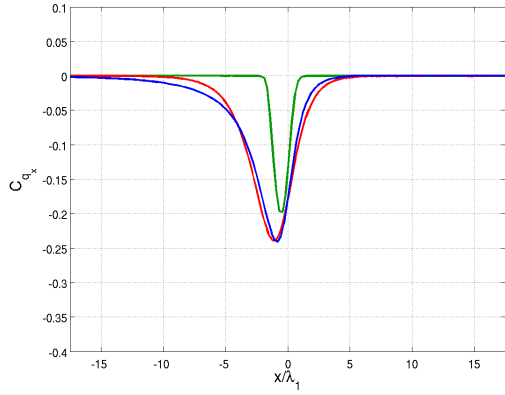
(a) $M_1 = 3.38$
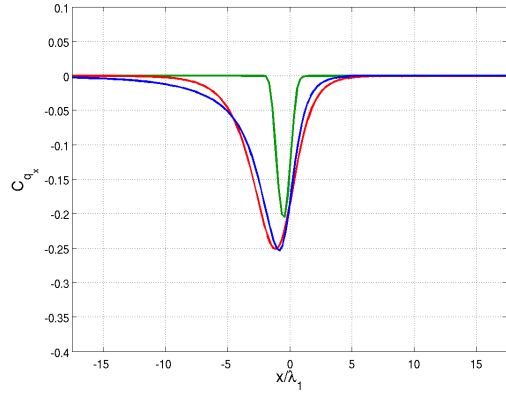
(b) $M_1 = 3.8$
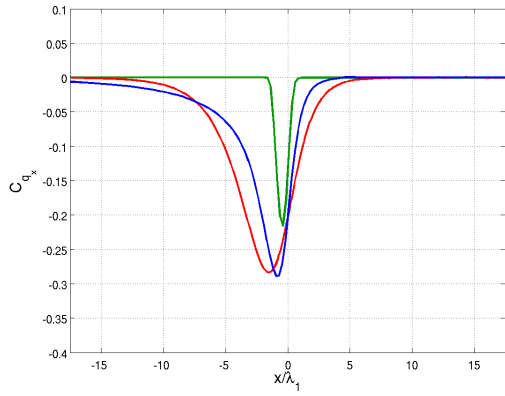
(c) $M_1 = 6.5$
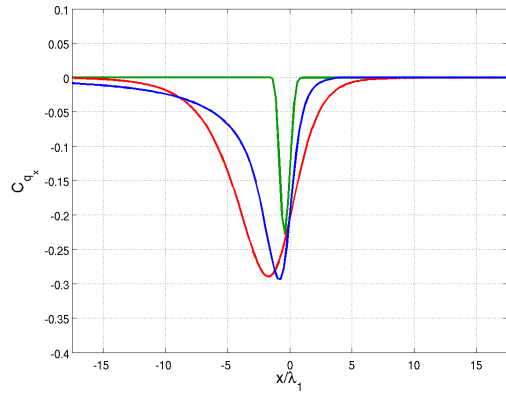
(d) $M_1 = 8.0$
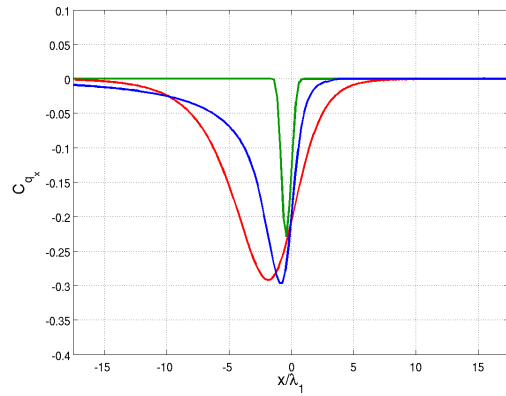
(e) $M_1 = 9.0$

Figure 20: Heat flux coefficient profiles for q_x in Argon. BGK & NS (blue); NS (green); DSMC (red).
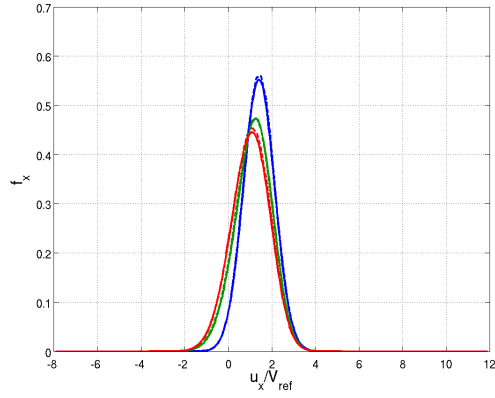
(a) $M_1 = 1.55$
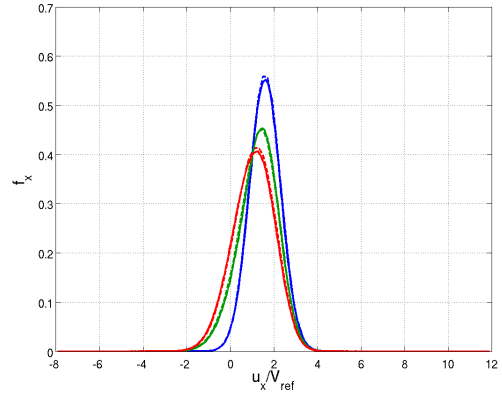
(b) $M_1 = 1.75$
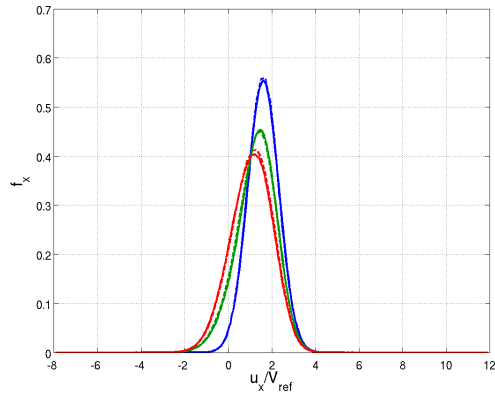
(c) $M_1 = 1.76$
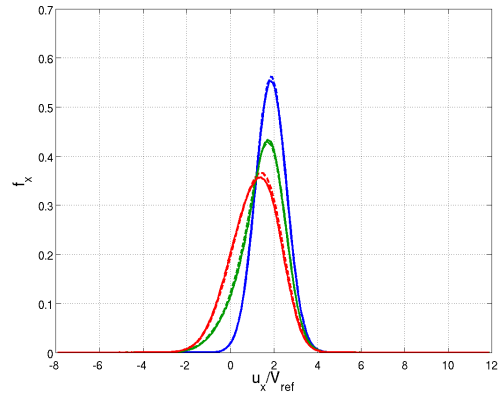
(d) $M_1 = 2.05$
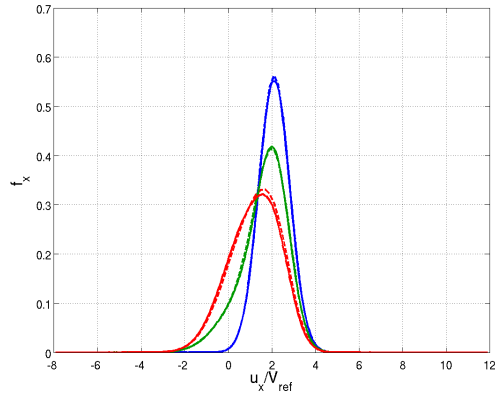
(e) $M_1 = 2.31$
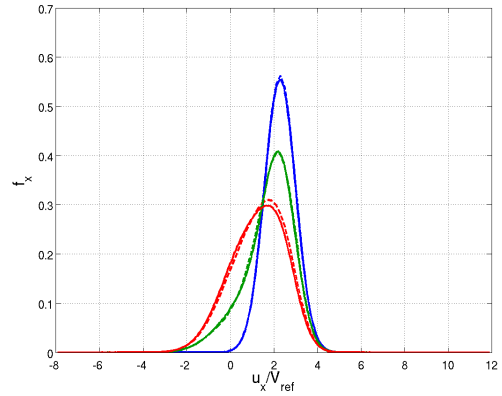
(f) $M_1 = 2.5$

Figure 21: Partially-integrated VDFs in Argon. $--$, BGK & NS; ——, DSMC. $x/\lambda_1 = -13.5$ (blue); $x/\lambda_1 = -1.5$ (green); $x/\lambda_1 = 0.0$ (red)

54
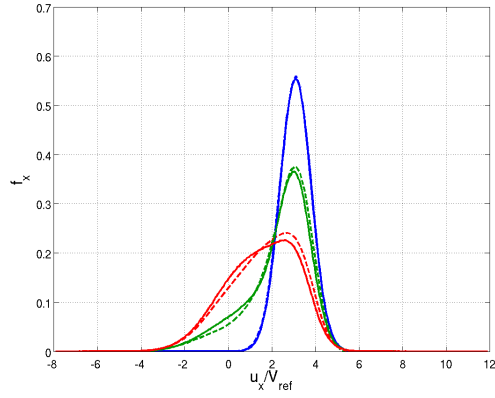
(a) $M_1 = 3.38$
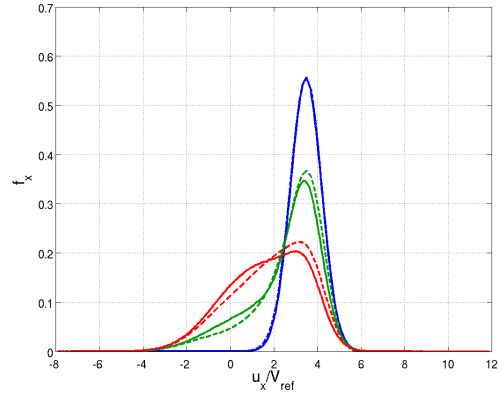
(b) $M_1 = 3.8$
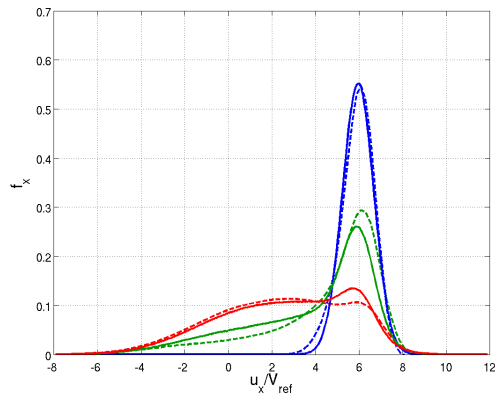
(c) $M_1 = 6.5$
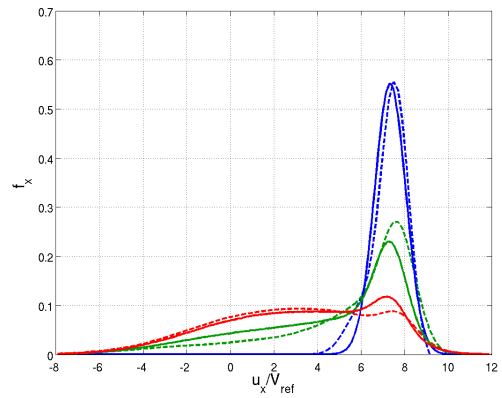
(d) $M_1 = 8.0$
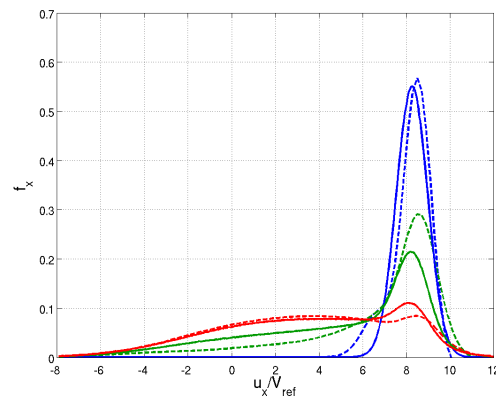
(e) $M_1 = 9.0$

Figure 22: Partially-integrated VDFs in Argon. $--$, BGK & NS; —, DSMC. $x/\lambda_1 = -13.5$ (blue); $x/\lambda_1 = -1.5$ (green); $x/\lambda_1 = 0.0$ (red)

55
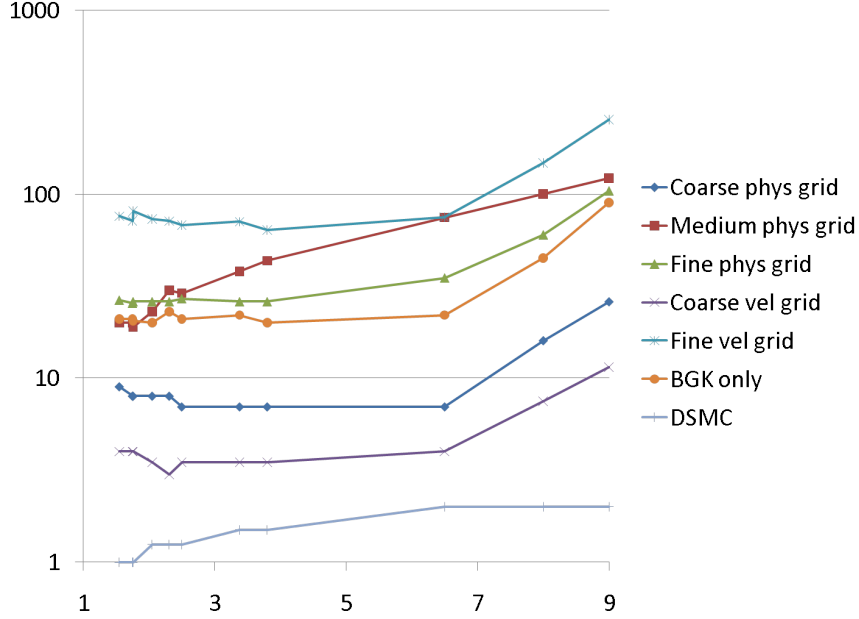
Figure 23: Total run times (in hours) versus M_1 for the Argon simulations on a semi-log scale.

hours ($61\times$ longer) for the medium grid. It must be noted that the DSMC solver uses a one-dimensional grid, whereas the UFS simulations require a two-dimensional grid. Also, the code DSMC1S was specifically designed to compute one-dimensional shock structures, while UFS is a general code meant to compute flowfields much more complex than just a one-dimensional shock. Therefore, it makes sense that UFS requires more computationally expensive than DSMC1S.

4.2   Nitrogen Shock Structure

Normalized density profiles in Nitrogen for various upstream Mach numbers have been presented by Alsmeyer, and are compared here with the results from UFS (coupled 3T-BGK & Euler solvers) in Figure 24 [3]. Also presented are results from UFS using the Euler solver in the entire domain, as well as DSMC results from Bird's code DSMC1S [6]. One immediately notices that the Euler results are atypical. A regular Euler solver predicts a very thin shock, whereas UFS's Euler solver shows a relaxation region downstream of the midpoint of the shock. This discrepancy may
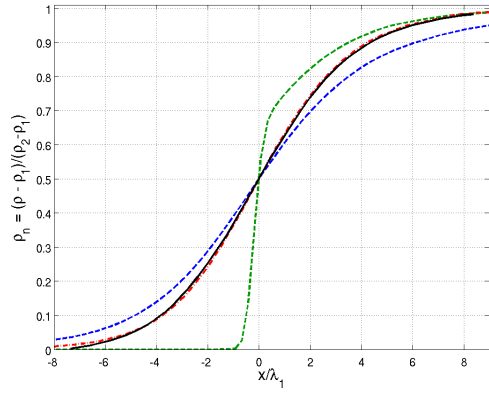
(a) $M_1 = 1.53$
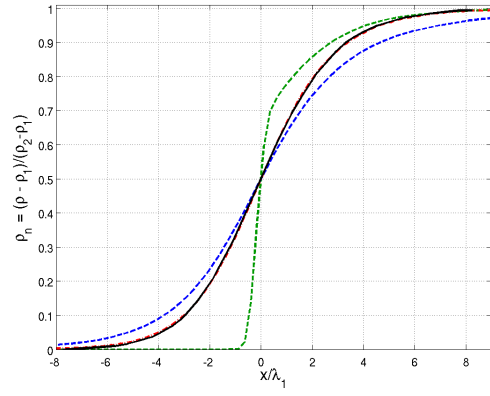
(b) $M_1 = 1.7$
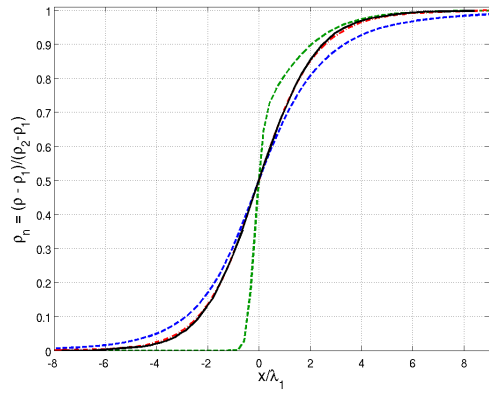
(c) $M_1 = 2.0$
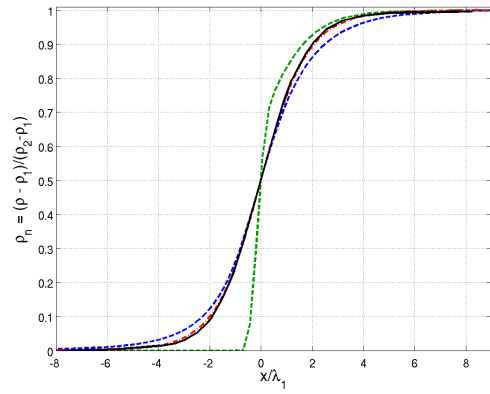
(d) $M_1 = 2.4$
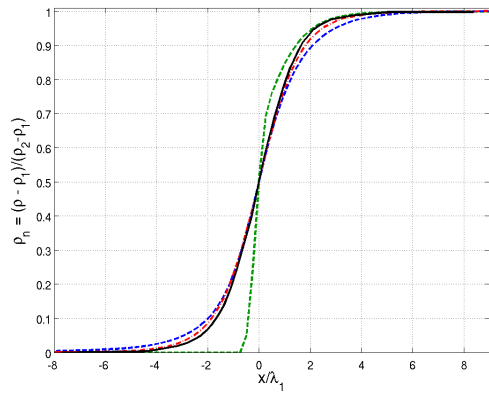
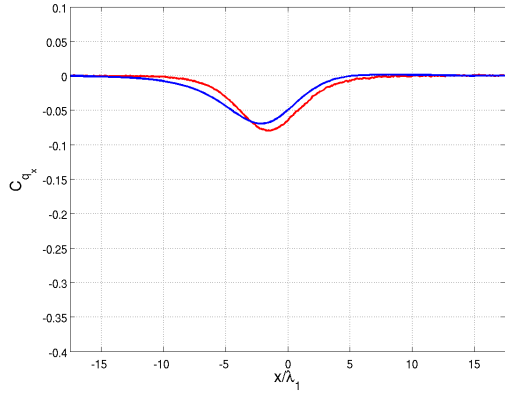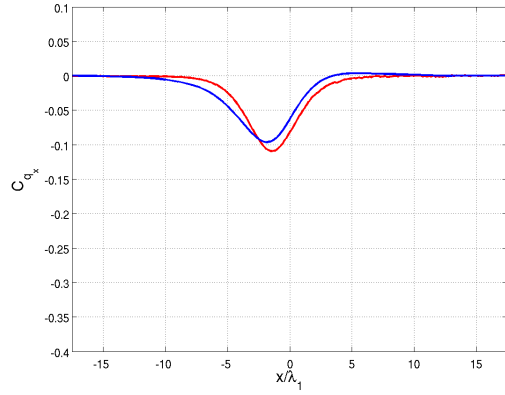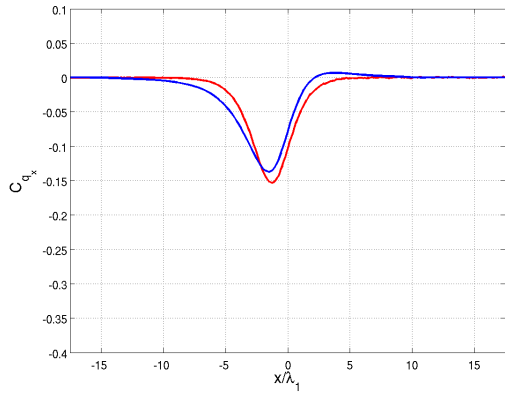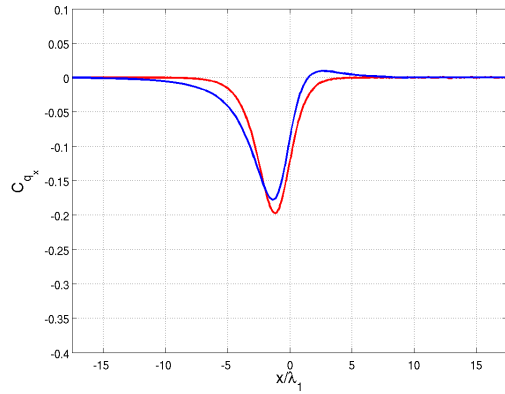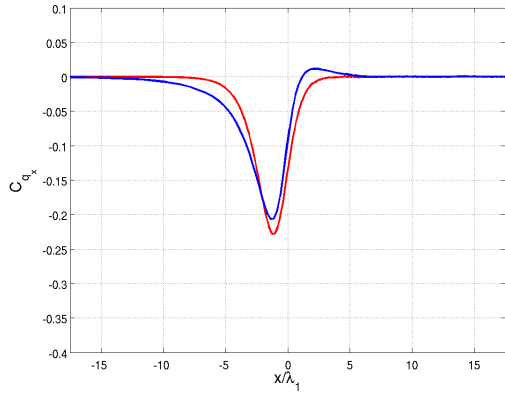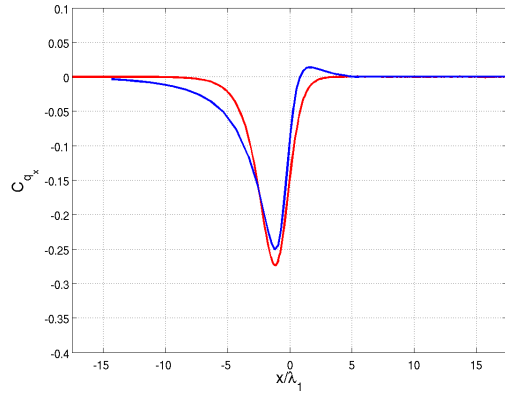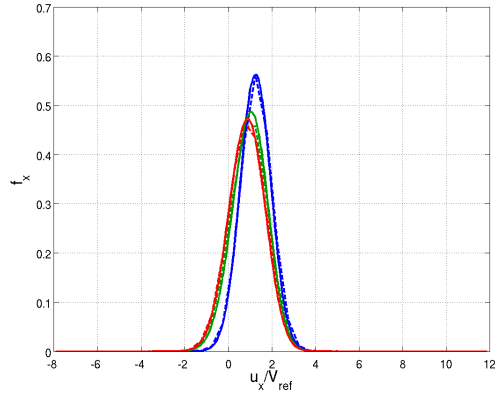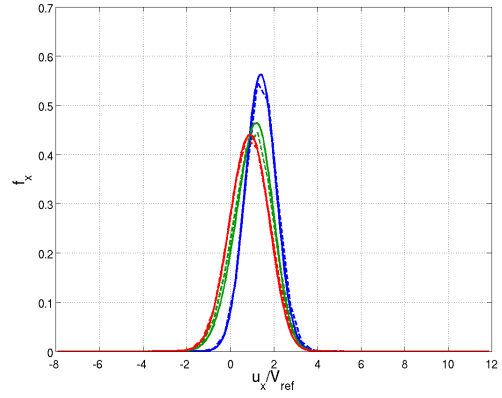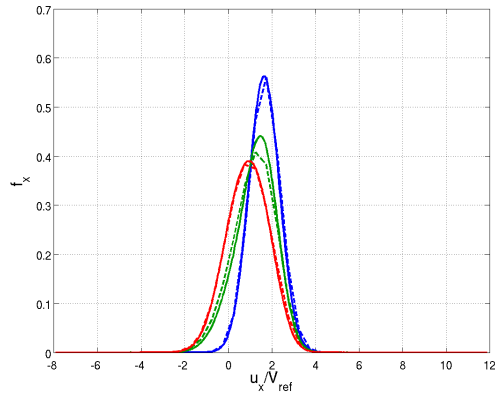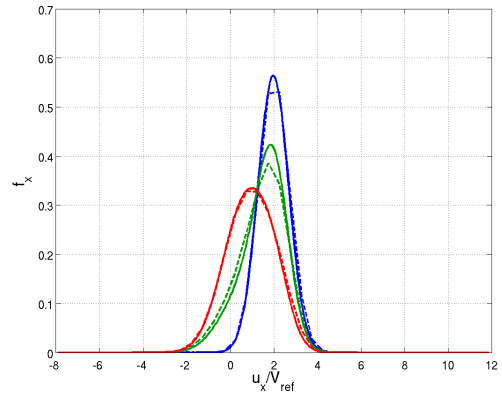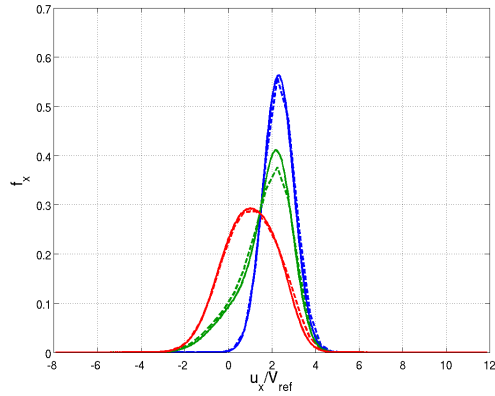(e) $M_1 = 2.8$
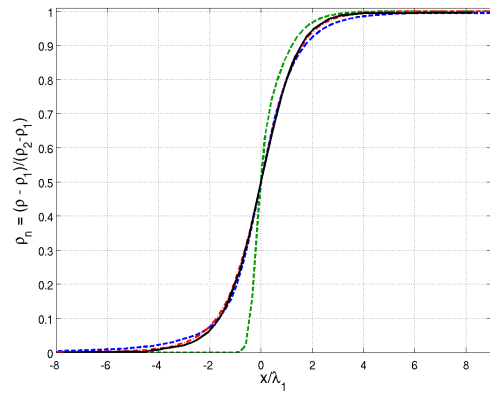
(f) $M_1 = 3.8$

Figure 24: Density profiles in Nitrogen. 3T-BGK & Euler (blue); Euler (green); DSMC (red); Alsmeyer (black).

be explained by the fact that the Euler solver in UFS is capable of accounting for internal energies, while a classical Euler solver is not. The developers have not yet published how the Euler solver was modified, so further explanation of these results must be deferred. The DSMC data closely match the experimental results, and the coupled solver predicts thicker shocks and, consequently, higher relaxation times. Agreement with the coupled solver and experiment improve with increasing upstream Mach number.

The inverse shock thickness is plotted in Figure 25; larger values indicate a thinner shock, and vice versa. DSMC agrees well with Alsmeyer's curve, even though
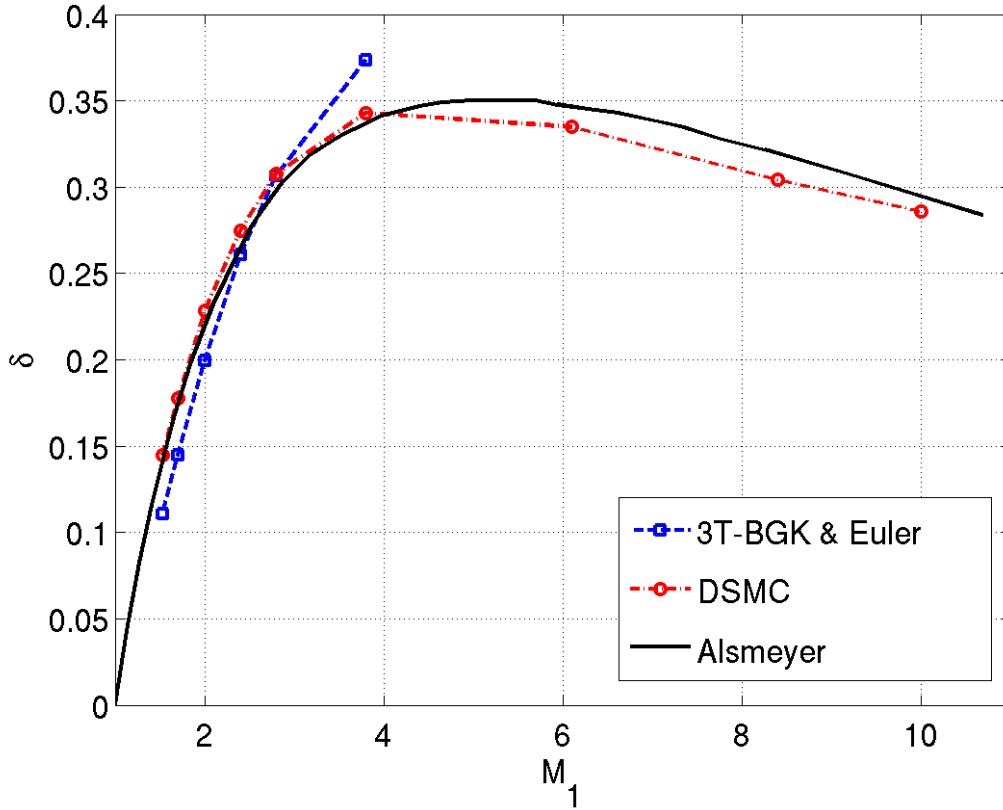
Figure 25: Inverse shock thickness δ for Nitrogen.

it overpredicts shock thickness for $M_1 > 4.0$. The 3T-BGK & Euler simulations show a similar trend as the BGK & NS simulations in Figure 15, since they predict

thinner shocks than experiment for $M_1 > 3$. The Euler results are not shown due to the atypical shock profiles given in Figure 24.

The density asymmetry factor is plotted in Figure 26 with experimental values from Alsmeyer for reference [3]. Even though Nitrogen simulations are here being
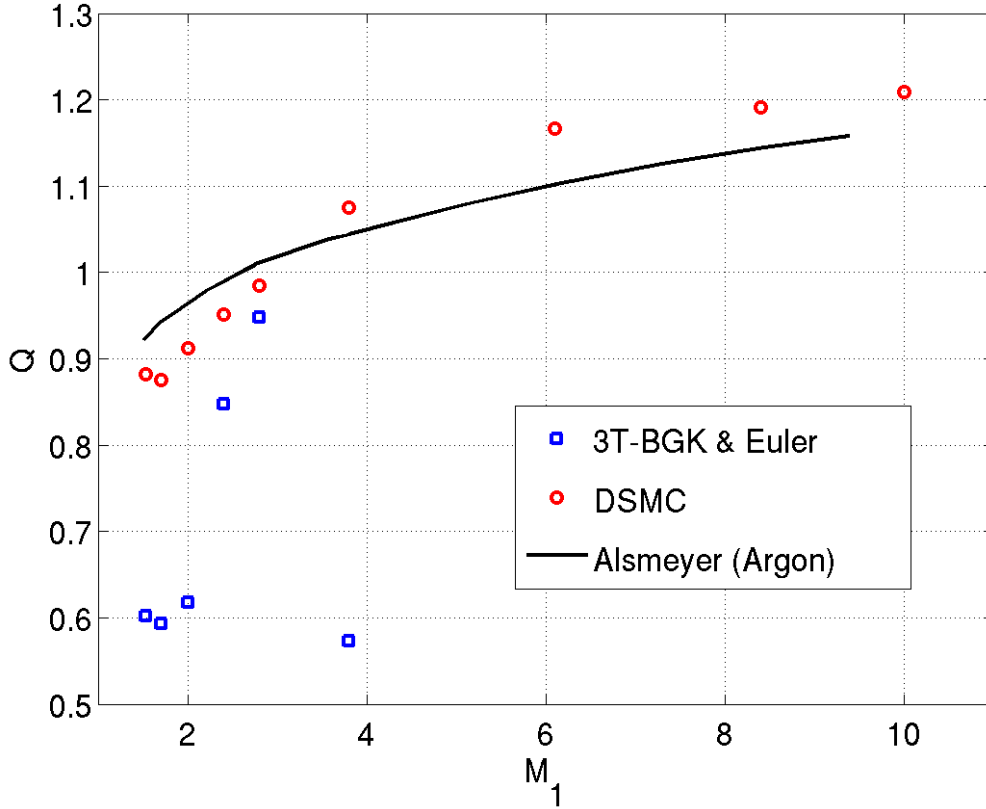
Figure 26: Density asymmetry Q in Nitrogen.

compared with Argon simulations, DSMC closely follows the Alsmeyer curve, while the coupled UFS solver (3T-BGK & Euler) agrees with DSMC for $M_1 > 2.0$.

As Nitrogen flows through the shock, the gas experiences translational, rotational, and vibrational nonequilibrium. The translational energy of a molecule is completely equilibrated after only one or two collisions, while it takes five and 79 million collisions for the rotational and vibrational energies to be completely transferred, respectively. As a result, T_{tr} not only equilibrates before T_{rot}, but T_{tr} may

be temporarily higher than its equilibrium value. This phenomenon occurs because it takes many more collisions for energy to be transferred to the rotational and vibrational modes, and yet the flow energy must go somewhere. Hence, the energy that will eventually go into rotational and vibrational excitation is temporarily stored as translational energy. The translational and rotational temperature profiles are shown in Figure 27. The coupled 3T-BGK & Euler solvers predict higher relaxation times for the rotational energy than does the DSMC solver. As a result, the coupled translational temperatures are higher than those for DSMC by as much as 2%.[2]

Heat flux coefficient C_{q_x} profiles are shown in Figure 28. The Euler simulations are not given since q_x is everywhere zero. For the upstream Mach numbers presented, the DSMC and 3T-BGK & Euler solvers differ at their minima by as much as 15%. The 3T-BGK & Euler solver also experiences a maximum between $1 < x/\lambda_1 < 5$, which is not apparent from the DSMC data. It is unclear whether this result is a numerical artifact of the 3T-BGK kinetic scheme, or whether DSMC is incorrectly predicting the heat flux, especially since there are arguments for both.[3]

The partially-integrated VDFs (f_x) are given in Figure 29. The coupled 3T-BGK & Euler solver shows very good agreement with the DSMC code. However, it is expected that a more refined velocity grid would give even better agreement, since the grid spacing here is $0.5V_{ref}$.

The total number of hours required to run each simulation (including the grid independence studies) is shown in Figure 30 versus the upstream Mach number M_1. At $M_1 = 1.53$ the time step is 5.05 μs, while at $M_1 = 3.8$ the time step is 2.81 μs.

For UFS, the run times are relatively constant up to $M_1 = 2.0$, at which point they increase exponentially, as shown on the logarithmic scale. The DSMC

---

[2]Comparison is made between dimensional temperatures.

[3]In Figure 27, the translational temperature experiences a maximum above the downstream equilibrium temperature, thus requiring a positive heat flux, justifying the 3T-BGK & Euler results. Alternatively, the energy captured in the translational temperature when it peaks goes into the rotational energy modes as the rotational temperature equilibrates, which requires only the heat flux predicted by the DSMC results.
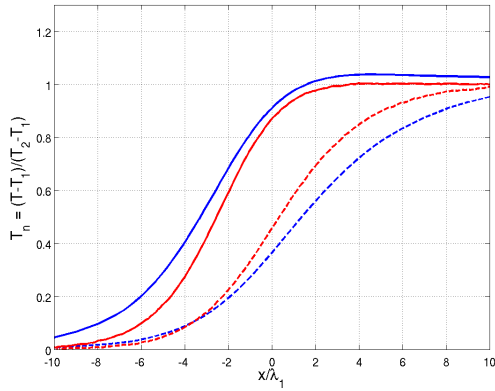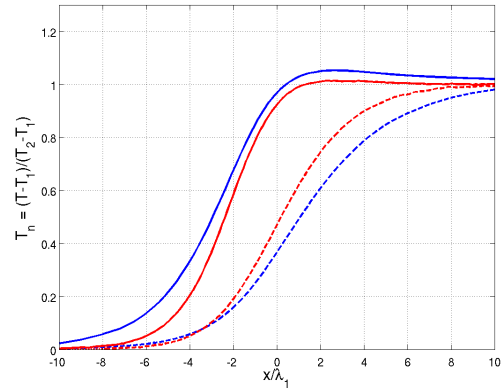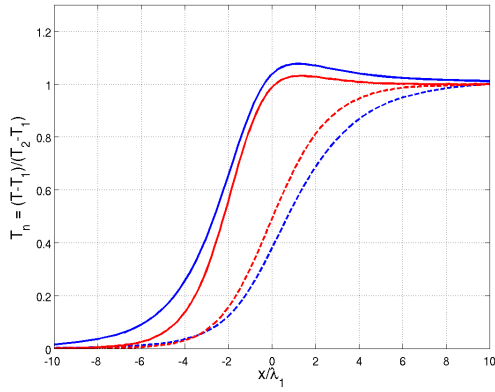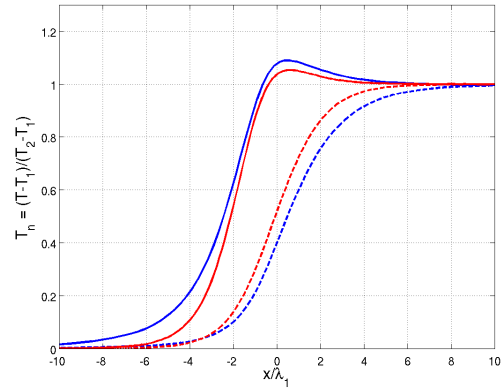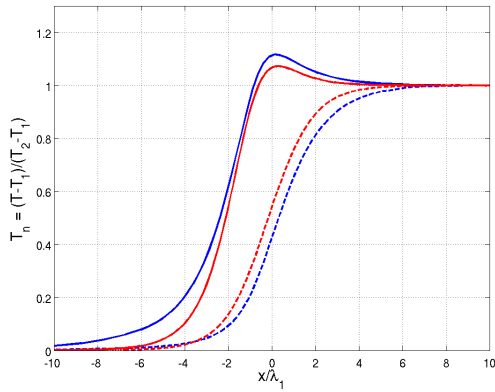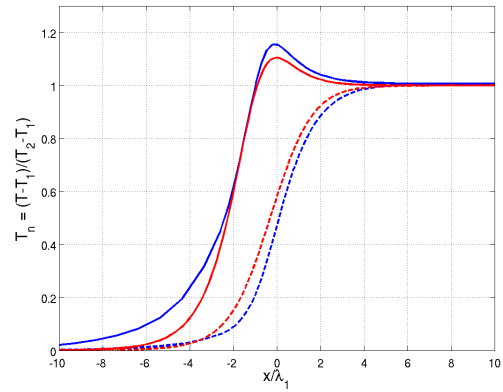
Figure 27: Translational and rotational temperature profiles in Nitrogen. —, T_{tr}; − −, T_{rot}; 3T-BGK & Euler (blue); DSMC (red).

(a) $M_1 = 1.53$

(b) $M_1 = 1.7$

(c) $M_1 = 2.0$

(d) $M_1 = 2.4$

(e) $M_1 = 2.8$

(f) $M_1 = 3.8$

Figure 28: Heat flux coefficient profiles for q_x in Nitrogen. 3T-BGK & Euler (blue); DSMC (red).

(a) $M_1 = 1.53$

(b) $M_1 = 1.7$

(c) $M_1 = 2.0$

(d) $M_1 = 2.4$

(e) $M_1 = 2.8$
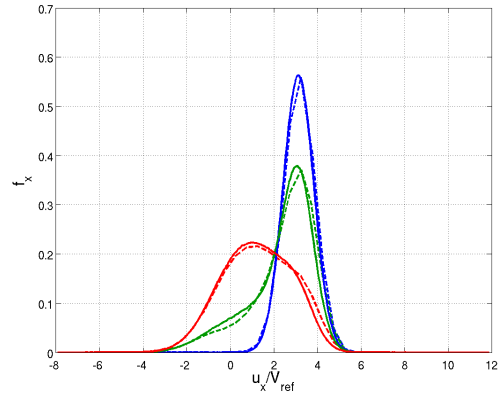
(f) $M_1 = 3.8$

Figure 29: Partially-integrated VDFs in Nitrogen. $--$, 3T-BGK & Euler; —, DSMC. $x/\lambda_1 = -13.5$ (blue); $x/\lambda_1 = -1.5$ (green); $x/\lambda_1 = 0.0$ (red)
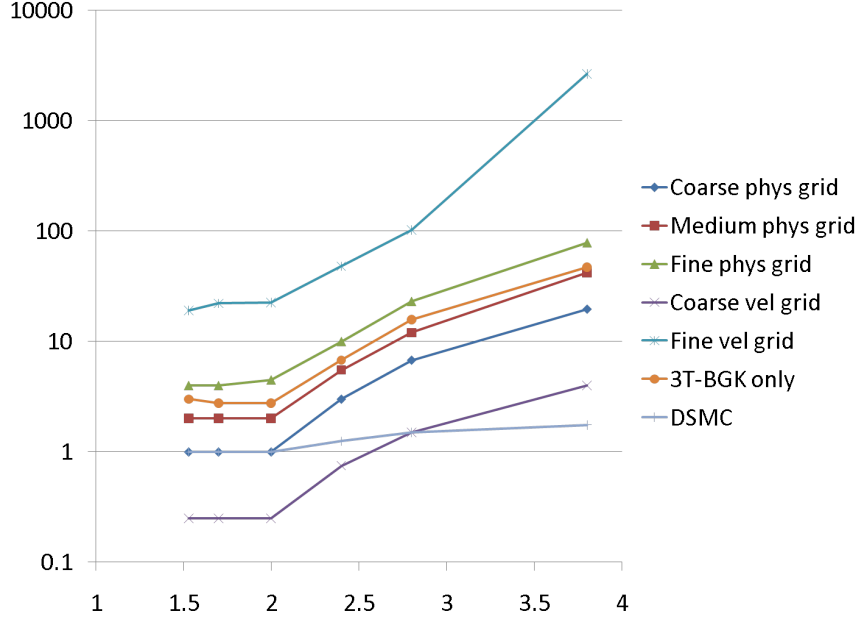
Figure 30: Total run times (in hours) versus M_1 for the Nitrogen simulations on a semi-log scale.

simulations took from 1 to 2 hours to complete, while the UFS simulations required up to 42 hours (24× longer) for the medium grid. The coarse and fine velocity grids bracket the UFS simulation times, showing that the most important factor in run times is the number of nodes in velocity space.

4.3 Entropy-Shock Interaction

The midpoint of the shock based on density moves as the entropy spot convects through the shock, and the entire shock actually is bowed, however slightly. Figure 31 gives the change in shock location for all three Knudsen numbers, where the non-dimensional time τ equals zero when the center of the entropy spot passes through $x/\lambda_1 = 0$. Since the center of the entropy spot is $5a$ upstream of the shock, τ is calculated as [12]

$$\tau \equiv \frac{t - 5\dfrac{a}{u_1}}{\dfrac{a}{u_1}}, \tag{80}$$

64

(a) All Kn (b) $Kn = 0.01$

(c) $Kn = 0.1$ (d) $Kn = 1.0$
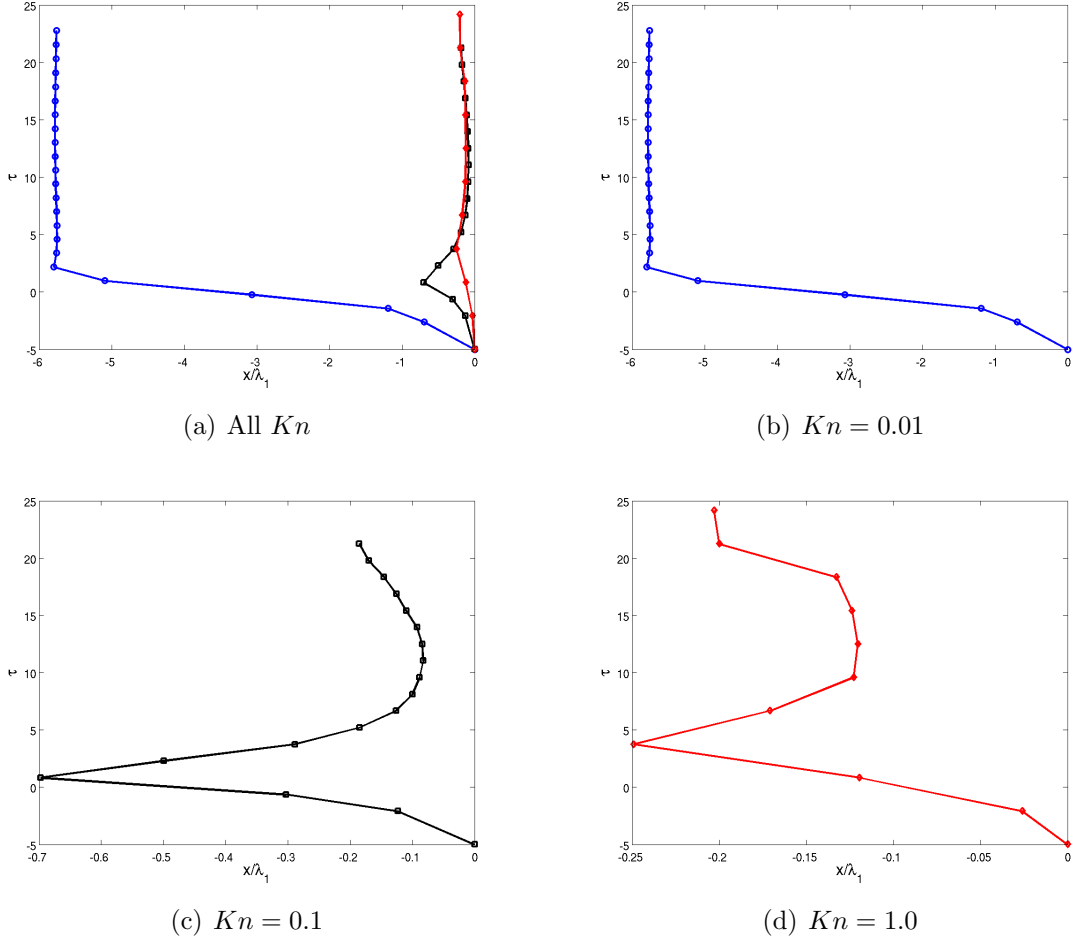
Figure 31: Shock locations as the simulation progresses in time (τ) for all three Knudsen numbers.

where t is the time (s), a is the radius of the entropy spot, and u_1 is the upstream x-direction velocity (m/s). Qualitatively, the shock location profiles exhibit the same behaviors, just on different scales. Even at $Kn = 0.01$, which is well into the continuum regime, the shock experiences a restoring force towards $x/\lambda_1 = 0$, albeit a small one. It is unclear why the shock does not return to its equilibrium location (as a completely normal shock) at $Kn = 0.01$. A possible explanation may be that the pressure wave, which emanates from the entropy spot after it has impinged with the shock, is more powerful at lower Knudsen numbers, causing the shock to be bowed

65

upstream. If this is the case, then the pressure wave at $Kn = 0.1$ and 1.0 is much weaker so as to allow the shock to almost completely be restored to a normal shock.

The density, pressure, and temperature profiles, as well as their gradient profiles, are shown in Figures 33, 34, and 35 for three different Knudsen numbers, $Kn = 0.01$, 0.1, and 1.0, respectively.

For $Kn = 0.01$, the density fluctuation is initially unaffected by the shock, with a post-shock strength of -20% at $\tau = 1.0$, damping out to -14% by $\tau = 20.3$. It is possible that with such a low Knudsen number, the shock thickness is not allowing the density fluctuation sufficient time to change. The temperature fluctuation, however is initially affected by the shock, which has a post-shock strength of only 20% (compared to a pre-shock strength of 25%) at $\tau = 1.0$, damping out to 14% at $\tau = 20.3$. It is interesting to note that even though the entropy spot does not induce any pressure fluctuations upstream of the shock, by convecting through the shock, the interaction creates a circular pressure wave (see [12]) centered about the symmetry plane. The pressure profile in Figure 33 shows a minimum of -5% at $\tau = 1.0$ which dampens to a minimum of -2% at $\tau = 5.8$. For $\tau > 5.8$, the pressure profile shows that there is a rarefaction region at the symmetry line. The numerical error introduced by the shock-symmetry boundary interface is apparent here near $x/a = 0$ since the flow parameters are relaxing from values above the downstream equilibrium values.

For $Kn = 0.1$, the shock thickness is larger than the simulation with $Kn = 0.01$. As a result, the density fluctuation is more affected initially by the shock, with a post-shock strength of -12% at $\tau = 0.8$, damping out to -7% by $\tau = 18.3$. The strength of the temperature fluctuation is cut in half to 12% at $\tau = 5.2$, damping out to 8% at $\tau = 20.3$. The pressure shows a minimum of -5% at $\tau = 0.8$ which dampens to a minimum of -1.5% at $\tau = 5.2$. For $\tau > 5.2$, the pressure profile indicates that there is actually a compression region after the shock at $Kn = 0.1$, which is in contrast to the rarefaction region predicted for $Kn = 0.01$. The numerical error introduced by the shock-symmetry boundary interface is again

apparent here near $x/a = 0$ since the flow parameters are relaxing from values above the downstream equilibrium values.

For $Kn = 1.0$, the shock thickness is larger still, apparent from the attenuation of the density fluctuation downstream of the shock (-7% at $\tau = 2.1$, dampened to -1.4% at $\tau = 9.6$). The numerical error from the shock-symmetry boundary is lessened at this Knudsen number (possibly due to the thicker shock), and so the flow parameters (except for pressure) are qualitatively showing correct behavior directly downstream of the shock (relaxing from values below the downstream equilibrium values). The strength of the temperature fluctuation is now only 4% at $\tau = 0.8$, damping out to 2% by $\tau = 9.6$. The pressure actually is exhibiting values above the downstream equilibrium value by 3% at $\tau = 0.8$, and 4% by $\tau = 9.6$, suggesting a compression region downstream of the shock.

The total number of hours required to run each simulation (including the grid independence studies) is shown in Figure 32 versus the Knudsen number Kn.
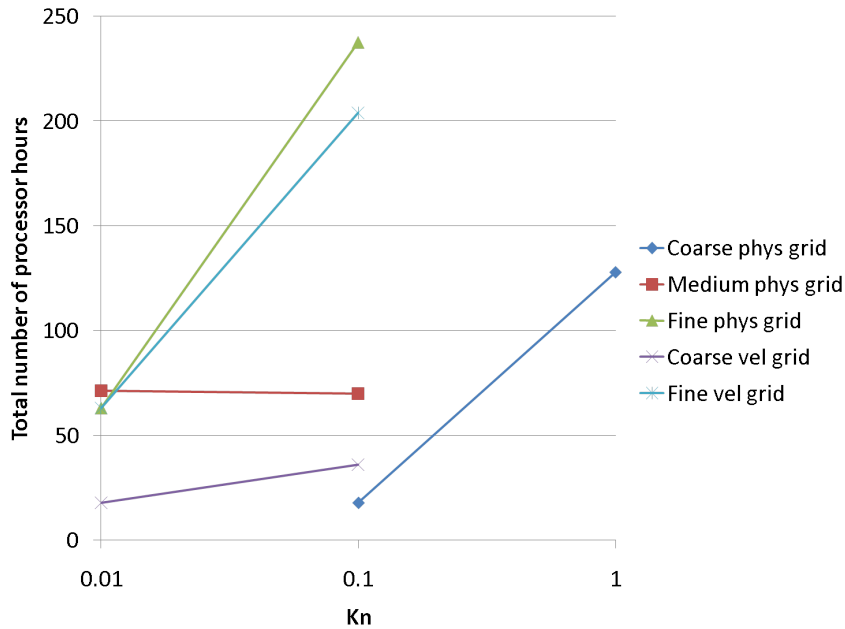
Figure 32: Total run times (in hours) versus Kn. The coarse and fine velocity grids use a medium physical grid, and the coarse and fine physical grids use a medium velocity grid.
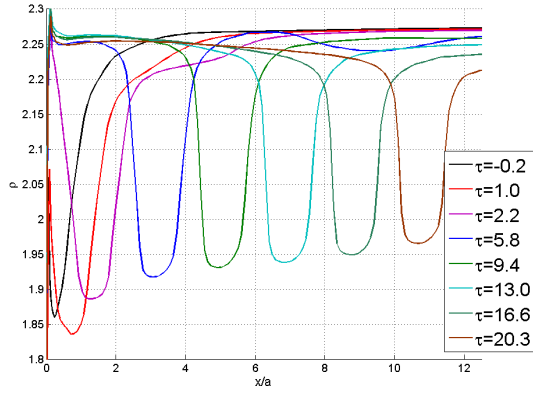
(a) Density
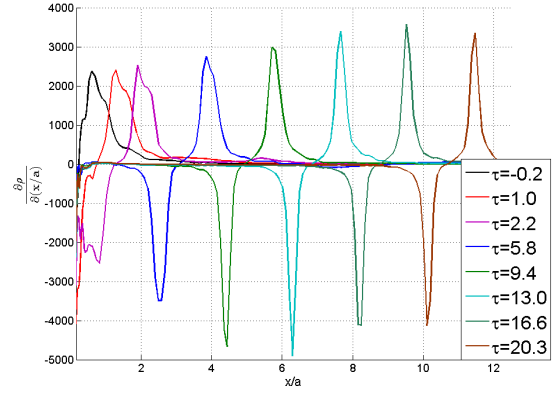
(b) Density gradients
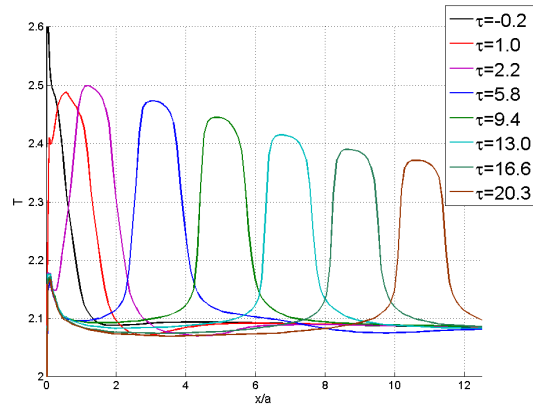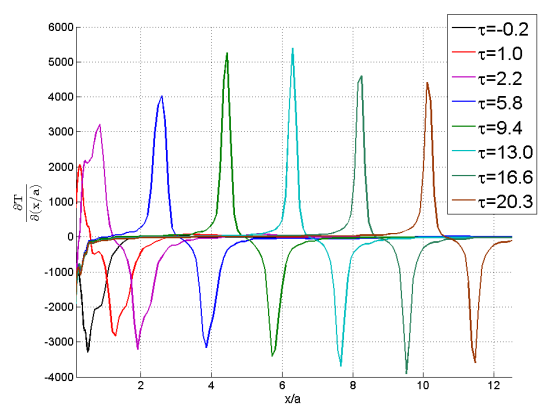
(c) Temperature

(d) Temperature gradients
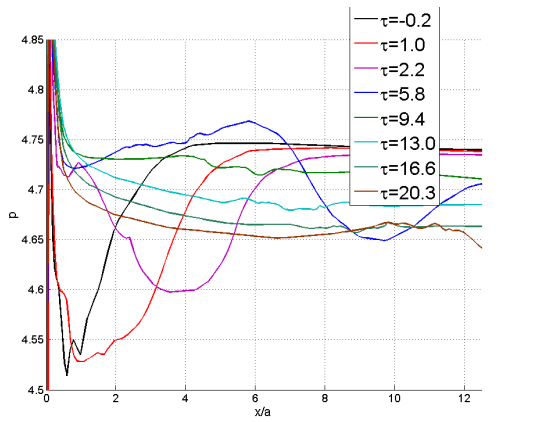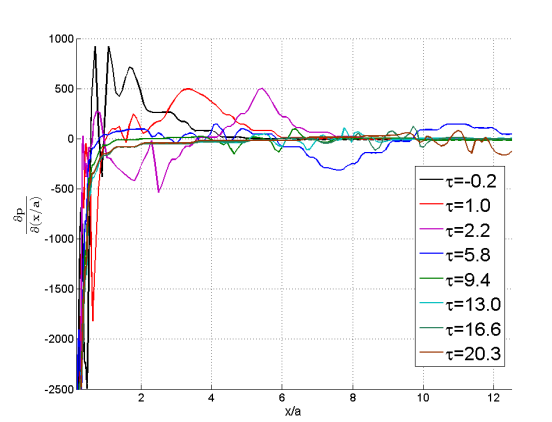
(e) Pressure

(f) Pressure gradients

Figure 33: Profiles for $Kn = 0.01$.
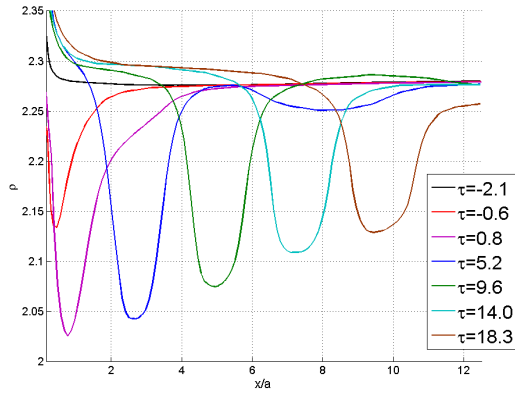
(a) Density
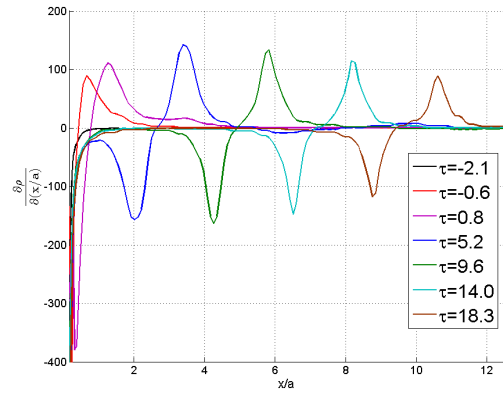
(b) Density gradients
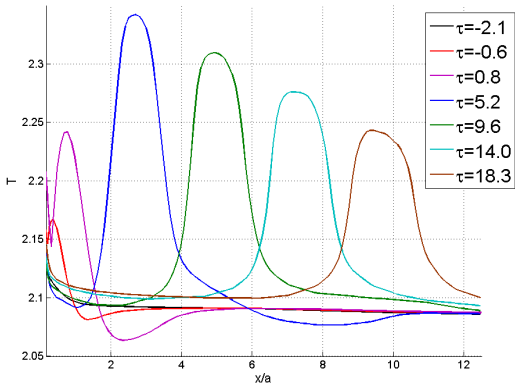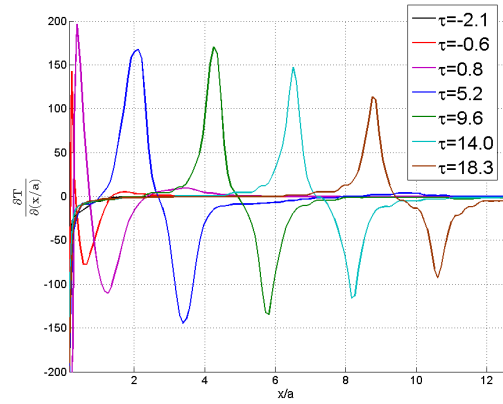
(c) Temperature

(d) Temperature gradients
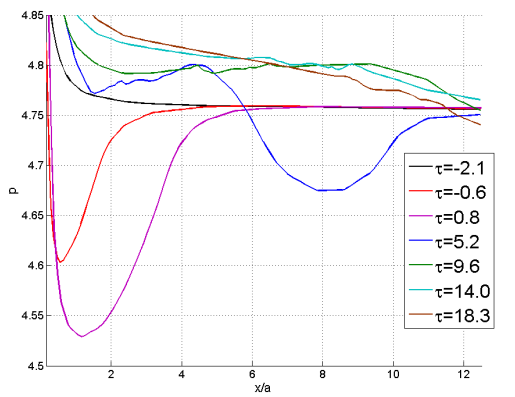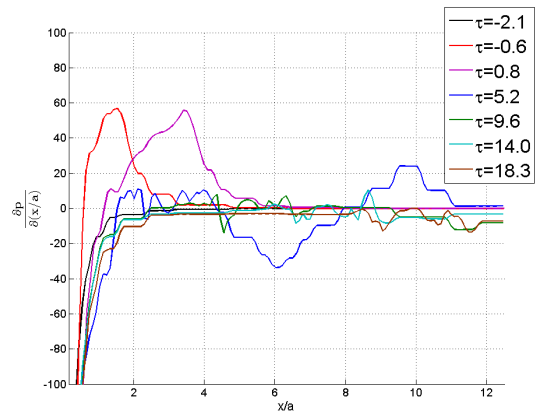
(e) Pressure

(f) Pressure gradients

Figure 34: Profiles for $Kn = 0.1$.
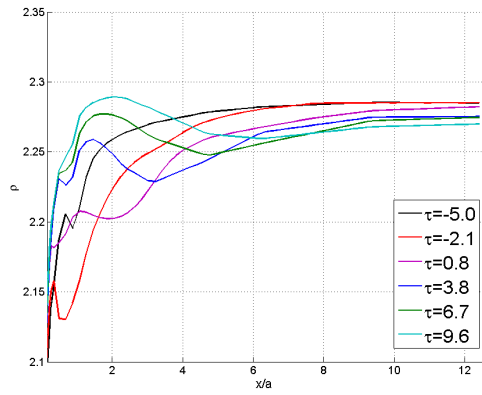
(a) Density
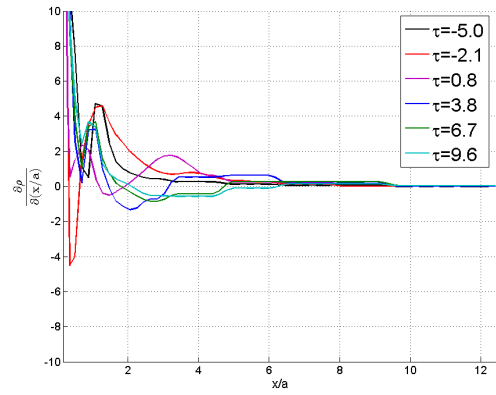
(b) Density gradients
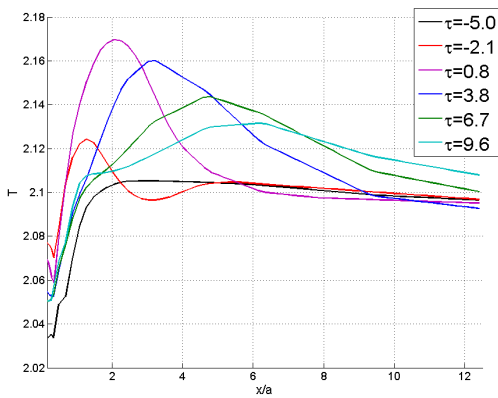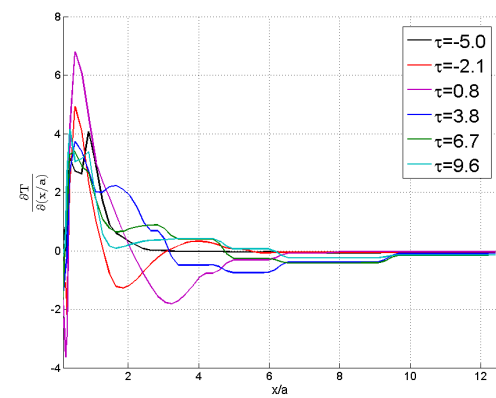
(c) Temperature

(d) Temperature gradients
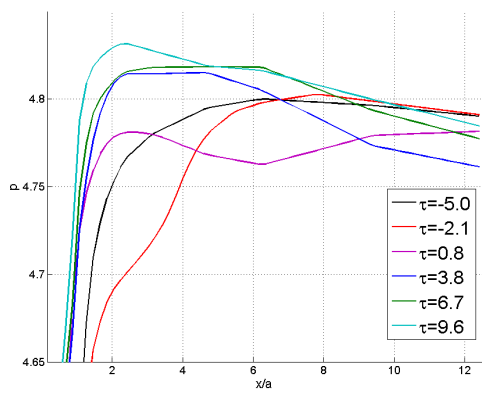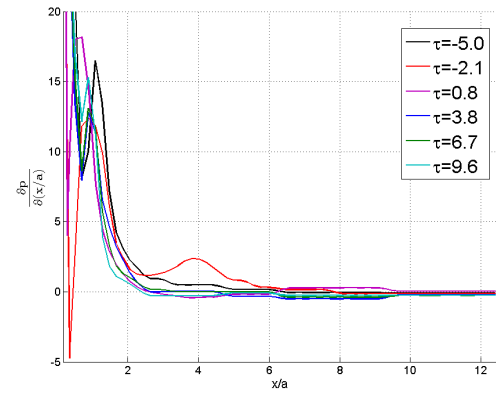
(e) Pressure

(f) Pressure gradients

Figure 35: Profiles for $Kn = 1.0$.

V. Conclusions

The schemes implemented in UFS (Euler, NS, BGK, and 3T-BGK) provide accurate results for one-dimensional simulations of shock structure in both Argon and diatomic Nitrogen. Profiles of density, temperatures, heat flux coefficient, and the partially-integrated VDF, as well as the shock thickness and the density asymmetry factor, show good agreement when compared with experimental results reported by Alsmeyer and with numerical simulations on Bird's DSMC1S code [3]. The Euler scheme in UFS gives atypical results, possibly due to its inclusion of internal energies. Coupling of continuum and kinetic solvers allows one to simulate a large flowfield while keeping computational cost down in flows with both continuum and rarefied regions. Further study of shock structure may include the other models and solution methods included in UFS (e.g. DNS of the collision integral, and various intermolecular potential models), and should utilize a one-dimensional grid in order to further reduce the computational cost required. Studies of additional continuum breakdown parameters may be made with comparison to this work.

Entropy-shock interactions continue to be an area of research, with the work presented here extending the analysis to NS and kinetic schemes. The shock moves upstream due to entropy-shock interactions, and seems to recover to a normal shock for higher Knudsen numbers ($Kn = 0.1$ and 1.0). Also, for $Kn = 0.01$, a rarefaction region is observed downstream of the shock, while for $Kn = 0.1$ and 1.0 a compression region is given. Numerical errors introduced where the shock and the symmetry boundary interface create uncertainty in the results presented. Further study should investigate the cause of this effect, and either use a full domain (instead of half of the domain with a symmetry boundary) or modify the symmetry boundary condition to eliminate the errors. As CFDRC improves the capabilities of UFS, especially the visualization software, the pressure waves downstream of the shock may be studied using pressure contours. VDFs may be studied by using a smaller value for the continuum breakdown parameter, or by performing the simulations with an uncoupled kinetic solver.

Appendix A: List of Symbols

73

74

Appendix B: List of Abbreviations

Bibliography

1. "Multi-national agreement to advance high-speed flight", AFRL News Release posted 14 Nov 2006 on Spaceflight Now, http://spaceflightnow.com/news/n0611/14hifire/.

2. Gerris Flow Solver, http://gfs.sourceforge.net.

3. Alsmeyer, H. "Density Profiles in Argon and Nitrogen Shock Waves Measured by the Absorption of an Electron Beam". *J. Fluid. Mech.*, 74, part 3:497–513, 1976.

4. Anderson, John D. *Hypersonic and High-Temperature Gas Dynamics.* American Institute of Aeronautics and Astronautics Inc., Reston, Virginia, 2nd ed. edition, 2006.

5. Anyiwo, Joshua C. and Dennis M. Bushnell. "Turbulence Amplification in Shock-Wave Boundary-Layer Interaction". *AIAA Journal*, 20(7):893–899, July 1982. AIAA 82-4170.

6. Bird, G. A. *Molecular Gas Dynamics and the Direct Simulation of Gas FLows.* Oxford University Press, Oxford, 1994.

7. Carr, Ryan W. *Quantifying Non-Equilibrium in Hypersonic Flows Using Entropy Generation.* Master's thesis, AFIT/GAE/ENY/07-M07, School of Engineering and Management, Air Force Institute of Technology (AU), Wright-Patterson AFB, OH, March 2007. (ADA469284).

8. Claycomb, Abram E. *Extending CFD Modeling to Near-Continuum Flows Using Enhanced Thermophysical Modeling.* Master's thesis, AFIT/GAE/ENY/08-M04, School of Engineering and Management, Air Force Institute of Technology (AU), Wright-Patterson AFB, OH, March 2008.

9. Duck, Peter W., D. Glenn Lasseigne, and M. Y. Hussaini. "On the Interaction Between the Shock Wave Attached to a Wedge and Freestream Disturbances". *Theoretical and Computational Fluid Dynamics*, 7:119–139, Feb 1995.

10. Duck, Peter W., D. Glenn Lasseigne, and M. Y. Hussaini. *The Effect of Three-Dimensional Freestream Disturbances on the Supersonic Flow Past a Wedge.* NASA Contractor Report 201698 ICASE Report No. 97-26, NASA, June 1997.

11. Fabre, David and Laurent Jacquin. "Linear Interaction of a Cylindrical Entropy Spot with a Shock". *Physics of Fluids*, 13(8):2403–2422, August 2001.

12. Grasso, F. and S. Pirozzoli. "Shock Wave-Thermal Inhomogeneity Interactions: Analysis and Numerical Simulations of Sound Generation". *Physics of Fluids*, 12(1):205–219, January 2000.

13. Grasso, F. and S. Pirozzoli. "Shock-Wave-Vortex Interactions: Shock and Vortex Deformations, and Sound production". *Theoretical and Computational Fluid Dynamics*, 13:421–456, 2000.

14. Harris, Stewart. *An Introduction to the Theory of the Boltzmann Equation*. Dover Publications, Inc., 1971. Originally published by Holt, Rinehart and Winston, Inc., New York.

15. Hussaini, M. Y., F. Collier, and D. M. Bushnell. "Turbulence Alteration Due to Shock Motion". *Turbulent Shear-Layer/Shock-Wave Interactions*, 371–381. Springer-Verlag, 1986.

16. Hussaini, M. Y. and G. Erlebacher. "Interaction of an Entropy Spot with a Shock". *AIAA Journal*, 37(3):346–356, March 1999.

17. Jain, P. C. "Rotational Collision Number for Nitrogen". *J. Phys. D: Appl. Phys.*, 13:25–28, 1980.

18. Josyula, Eswar, William F. Bailey, and Kun Xu. "Nonequilibrium Relaxation in High Speed Flows". *37th AIAA Thermophysics Conference*, June 2004. AIAA 2004-2468.

19. Josyula, Eswar, Kun Xu, and Dean C. Wadsworth. "Testing Continuum and Non-Continuum Descriptions in High Speed Flows". M. Capitelli (editor), *Rarefied Gas Dynamics: 24th International Symposium*, 1217–1222. 2005.

20. Kolobov, V., V. Aristov, R. Arslanbekov, S. Bayyuk, A. Frolova, and S. Zabelok. "Construction of a Unified Continuum/Kinetic Solver for Aerodynamic Problems". *Journal of Spacecraft and Rockets*, 42:598–606, July 2005.

21. Kolobov, V.I., R.R. Arslanbekov, V.V. Aristov, A.A. Frolova, and S.A. Zabelok. "Unified Solver for Rarefied and Continuum Flows with Adaptive Mesh and Algorithm Refinement". *Journal of Computational Physics*, 223:589–608, 2007.

22. Kolobov, Vladimir I., Robert R. Arslanbekov, Vladimir V. Aristov, Anna A. Frolova, and Sergey A. Zabelok. "Unified Flow Solver for Aerospace Applications". *44th AIAA Aerospace Sciences Meeting and Exhibit*. January 2006. AIAA 2006-988.

23. Li, Qibing, Song Fu, and Kun Xu. "A Compressible Navier-Stokes Flow Solver with Scalar Transport". *Journal of Computational Physics*, 204(2):692 – 714, 2005. ISSN 0021-9991.

24. May, Georg, Balaji Srinivasan, and Antony Jameson. "An Improved Gas-Kinetic BGK Finite-Volume Method for Three-Dimensional Transonic Flow". *Journal of Computational Physics*, 220(2):856 – 878, 2007. ISSN 0021-9991.

25. McKenzie, J. F. and K. O. Westphal. "Interaction of Linear Waves with Oblique Shock Waves". *The Physics of Fluids*, 11(11):2350–2362, November 1968.

26. Meadows, K., A. Kumar, and M. Hussaini. "A Computational Study on the interaction Between a Vortex and a Shock Wave". *AIAA 12th Aeroacoustics Conference*, 1989. AIAA-89-1043.

27. Millikan, Roger C. and Donald R. White. "Systematics of Vibrational Relaxation". *The Journal of Chemical Physics*, 39(12):3209–3213, December 1963.

28. Moore, Franklin K. *Unsteady Oblique Interaction of a Shock Wave with a Plane Disturbance*. Technical Report Report 1165, NACA, 1954.

29. Nanbu, K. and Y. Watanabe. *Analysis of the Internal Structure of Shock Waves by Means of the Exact Direct-Simulation Method*. Technical report, Institute of High Speed mechanics, Tohoku University, 1984.

30. Ohwada, Taku. "Structure of Normal Shock Waves: Direct Numerical Analysis of the Boltzmann Equation for Hard-Sphere Molecules". *Physics of Fluids A: Fluid Dynamics*, 5(1):217–234, 1993.

31. Ribner, H. S. *Convection of a Pattern of Vorticity Through a Shock Wave*. Technical Report Report 1164, NACA, 1954.

32. Roveda, Roberto, David B. Goldstein, and Philip L. Varghese. "Hybrid Euler/Direct Simulation Monte Carlo Calculation of Unsteady Slit Flow". *Journal of Spacecraft and Rockets*, 37(6):753–760, November-December 2000.

33. Schmidt, B. "Electron Beam Density Measurements in Shock Waves in Argon". *J. Fluid Mech.*, 39:361–373, 1969.

34. Schrock, Christopher R. *Entropy Generation as a Means of Examining Continuum Breakdown*. Master's thesis, AFIT/GAE/ENY/05-M20, School of Engineering and Management, Air Force Institute of Technology (AU), Wright-Patterson AFB, OH, March 2005. (ADA436456).

35. Simon, Charles E. *Higher Order Gasdynamic Theory of Shock Structure*. Ph.D. thesis, University of Colorado, Dec 1977.

36. Sone, Yoshio. *Kinetic Theory and Fluid Dynamics*. Birkhauser, 2002.

37. Vincenti, Walter G. and Charles H. Kruger. *Introduction to Physical Gas Dynamics*. John Wiley & Sons Inc., New York, 1st ed. edition, 1965.

38. White, Frank M. *Viscous Fluid Flow*. McGraw-Hill, 3rd edition, 2006.

39. Xu, Kun. "A Gas-Kinetic BGK Scheme for the Navier-Stokes Equations and Its Connection with Artificial Dissipation and Godunov Method". *Journal of Computational Physics*, 171:289–335, 2001.

40. Xu, Kun and Zhaoli Guo. "Generalized Gas Dynamic Equations". *47th AIAA Aerospace Sciences Meeting Including The New Horizons Forum and Aerospace Exposition*, January 2009. AIAA 2009-672.

41. Zang, Thomas A., M. Y. Hussaini, and Dennis M. Bushnell. "Numerical Computations of Turbulence Amplification in Shock-Wave Interactions". *AIAA Journal*, 22(1):13–21, January 1984.

42. Zel'dovich, Yakov B. and Yu. P. Raizer. *Physics of Shock Waves and High-Temperature Hydrodynamic Phenomena*. Dover, New York, 2002.

Vita

Lieutenant Brook Bentley served as a proselyting missionary in Poland for two years beginning in 1999. He then received his Bachelor's degree in Mechanical Engineering in 2005 from Brigham Young University. After graduating from Officer Training School at Maxwell Air Force Base, Alabama, he supported the F-22 program at Wright-Patterson Air Force Base as the Lead Support Equipment Engineer. Currently, he is pursuing a Master's degree in Aeronautical Engineering from the Air Force Institute of Technology. Upon graduation, he will be assigned to Kirtland Air Force Base where he will serve in the Laser Effects Branch of the Directed Energy Directorate, Air Force Research Laboratory.

REPORT DOCUMENTATION PAGE

Form Approved
OMB No. 0704–0188

1. REPORT DATE (DD–MM–YYYY) 26-03-2009	2. REPORT TYPE Master's Thesis	3. DATES COVERED (From — To) Sep 2007 – Mar 2009

4. TITLE AND SUBTITLE	5a. CONTRACT NUMBER
An Investigation of Shock Wave Physics via Hybrid CFD-BGK Solution Methods for Nonequilibrium Flows	
	5b. GRANT NUMBER
	5c. PROGRAM ELEMENT NUMBER

6. AUTHOR(S)	5d. PROJECT NUMBER
Bentley, Brook I., 1st Lt, USAF	JON# 09ENY125
	5e. TASK NUMBER
	5f. WORK UNIT NUMBER

7. PERFORMING ORGANIZATION NAME(S) AND ADDRESS(ES) Air Force Institute of Technology Graduate School of Engineering and Management (AFIT/ENY) 2950 Hobson Way WPAFB OH 45433-7765	8. PERFORMING ORGANIZATION REPORT NUMBER AFIT/GAE/ENY/09-M02

9. SPONSORING / MONITORING AGENCY NAME(S) AND ADDRESS(ES) Air Vehicles Directorate, Air Force Research Laboratory Attn: Dr. Datta V. Gaitonde 2210 8th St. B146 R225 WPAFB, OH 45433 (937) 904-4031 (DSN: 674-4031)	10. SPONSOR/MONITOR'S ACRONYM(S) AFRL/RBAC
	11. SPONSOR/MONITOR'S REPORT NUMBER(S)

12. DISTRIBUTION / AVAILABILITY STATEMENT
APPROVED FOR PUBLIC RELEASE; DISTRIBUTION UNLIMITED

13. SUPPLEMENTARY NOTES
This material is declared a work of the U.S. Government and is not subject to copyright protection in the United States.

14. ABSTRACT

The Unified Flow Solver, a hybrid continuum-rarefied code, is used to investigate the internal structure of a normal shock wave for a Mach range of 1.55 to 9.0 for Argon, and 1.53 to 3.8 for diatomic Nitrogen. Reciprocal shock thickness, density, temperature, heat flux, and the velocity distribution function are calculated for a one-dimensional shock wave and compared with experimental data from Alsmeyer and DSMC results from Bird. Using the Euler, Navier-Stokes, BGK model, and Three-Temperature BGK model schemes, results from UFS compare well with experiment and DSMC. The Euler scheme shows atypical results, possibly resulting from modifications made to include internal energies.

An entropy spot is introduced into a two-dimensional domain to investigate entropy-shock interactions over a range of Knudsen numbers (Kn=0.01, 0.1, and 1.0) for Mach 2.0 in Argon. Previous work on entropy-shock interactions has only been performed using an Euler scheme. Here, results are presented in Argon using coupled BGK and Navier-Stokes solvers. Density, pressure, and temperature profiles, as well as the profiles of their gradients, are reported at certain times after the entropy spot convects through the shock.

15. SUBJECT TERMS
Hypersonic, Nonequilibrium, Entropy, Shock Structure, BGK

16. SECURITY CLASSIFICATION OF:			17. LIMITATION OF ABSTRACT	18. NUMBER OF PAGES	19a. NAME OF RESPONSIBLE PERSON Robert B. Greendyke, AFIT/ENY
a. REPORT	b. ABSTRACT	c. THIS PAGE	UU	92	19b. TELEPHONE NUMBER (Include Area Code) (937) 255-3636 x4567 Robert.Greendyke@afit.edu
U	U	U			

Standard Form 298 (Rev. 8–98)
Prescribed by ANSI Std. Z39.18